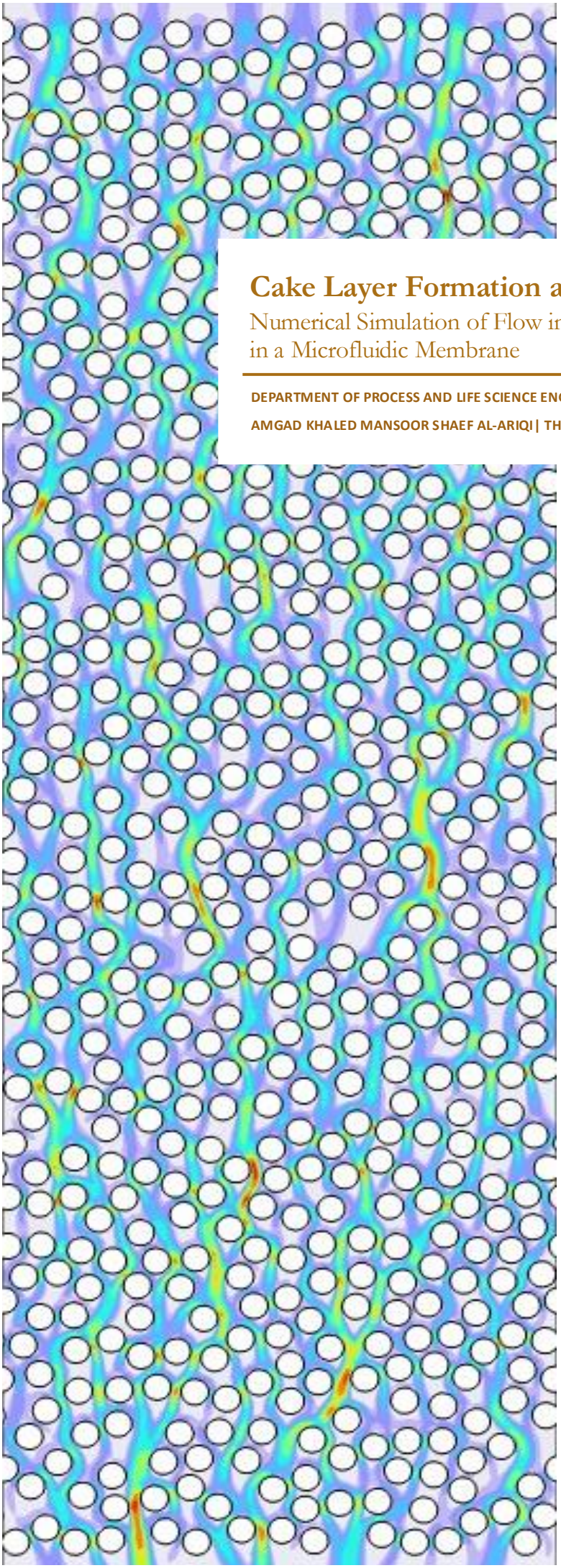

Cake Layer Formation and Filtration of Soft Particles

Numerical Simulation of Flow in Porous Media: Permeability of Micropillar Arrays in a Microfluidic Membrane

DEPARTMENT OF PROCESS AND LIFE SCIENCE ENGINEERING | LUND UNIVERSITY

AMGAD KHALED MANSOOR SHAEF AL-ARIQI | THESIS 2025

Cake Layer Formation and Cake Filtration of Soft Particles

(Numerical Simulation of Flow in Porous Media: Permeability of Micropillar Arrays in a Microfluidic Membrane)

by

Amgad Khaled Mansoor Shaef Al-ariqi

Division of Chemical Engineering
Department of Process and Life Science Engineering
Lund University

August 2025

Supervisor: **Professor Frank Lipnizki**
Co-supervisor: **Professor Rob Lammertink**
Examiner: **Professor Ola Wallberg**

Picture on front page: Membrane velocity distributions generated using COMSOL Multiphysics®.

Postal address	**Visiting address**	**Telephone**
Box 124	Kemicentrum	+46 46-222 82 85
SE-221 00 Lund, Sweden	Naturvetarvägen 22	+46 46-222 00 00
Web address	223 62 Lund, Sweden	
http://www.ple.lth.se		

Membrane Engineering for Sustainable Development

Funded by the European Union

Acknowledgment

This master thesis project has been conducted as part of the Erasmus Mundus Joint Master in *Membrane Engineering for Sustainable Development, MESD*, funded by the European Union.

The author thanks the European Commission - Education, Audiovisual and Culture Executive Agency (EACEA) for the Erasmus Mundus scholarship under the program: Master in Membrane Engineering for Sustainable Development, MESD), Project number: 101081874, Call: ERASMUS-EDU-2022-PEX-EMJM-MOB

EN	Funded by the European Union. Views and opinions expressed are however those of the author(s) only and do not necessarily reflect those of the European Union or the European Education and Culture Executive Agency (EACEA). Neither the European Union nor EACEA can be held responsible for them.
FR	Financé par l'Union européenne. Les points de vue et avis exprimés n'engagent toutefois que leur(s) auteur(s) et ne reflètent pas nécessairement ceux de l'Union européenne ou de l'Agence exécutive européenne pour l'éducation et la culture (EACEA). Ni l'Union européenne ni l'EACEA ne sauraient en être tenues pour responsables
NL	Gefinancierd door de Europese Unie. De hier geuite ideeën en meningen komen echter uitsluitend voor rekening van de auteur(s) en geven niet noodzakelijkerwijs die van de Europese Unie of het Europese Uitvoerende Agentschap onderwijs en cultuur (EACEA) weer. Noch de Europese Unie, noch het EACEA kan ervoor aansprakelijk worden gesteld.
SV	Finansieras av Europeiska unionen. De synpunkter och åsikter som uttrycks är endast upphovsmannens [upphovsmännens] och utgör inte Europeiska unionens eller Europeiska genomförandeorganet för utbildning och kulturs (EACEA) officiella ståndpunkt. Varken Europeiska unionen eller EACEA tar något ansvar för dessa.
ES	Financiado por la Unión Europea. Las opiniones y puntos de vista expresados solo comprometen a su(s) autor(es) y no reflejan necesariamente los de la Unión Europea o los de la Agencia Ejecutiva Europea de Educación y Cultura (EACEA). Ni la Unión Europea ni la EACEA pueden ser considerados responsables de ellos.

Preface

In the name of Allah, the Most Gracious, the Most Merciful. All praise and gratitude are due to Allah for the countless blessings, strength, and guidance that have illuminated my path throughout this academic journey.

This master's thesis represents the culmination of dedicated research and a significant period of personal and academic growth. The completion of this work would not have been possible without the support and guidance of many individuals to whom I am deeply indebted.

I would like to express my sincerest gratitude to my supervisor, Professor Frank Lipnizki. His expertise, insightful feedback, and unwavering encouragement were instrumental in shaping the direction of this research.

A significant portion of this work was conducted during my master's thesis internship at the University of Twente, and for this invaluable opportunity, I am deeply grateful. I extend my profound thanks to my co-supervisor, Professor Rob Lammertink, with whom I had the privilege of working closely. His critical perspective and guidance greatly enriched this study. My sincere appreciation also goes to Ermia Azari Moghaddam for his consistent support, collaborative discussions, and assistance throughout my time in the University of Twente.

I owe a special and heartfelt debt of gratitude to my family. Their endless love, unwavering support, and constant encouragement have been my foundation throughout my life and academic pursuits.

I extend my appreciation to my colleagues for creating a stimulating and supportive environment. Your companionship and intellectual engagement have made this journey both enjoyable and rewarding.

Finally, I would like to acknowledge the Erasmus Mundus Joint Master in Membrane Engineering for a Sustainable Development (MESD). I am grateful to the program staff and coordinators for their exceptional organization and support.

Dedication

To my family—
whose unwavering love has been my anchor,
whose boundless support has been my compass,
and whose constant encouragement lit the path through every challenge,
this work is as much yours as it is mine.
Thank you for believing in me.

لكم الفضل بعد الله في كل ما وصلت إليه، فشكراً لكم من القلب **...**

Popular Scientific Summary

In industries from water purification to food production, a major problem called "membrane fouling" can increase energy consumption by over 50% and significantly raise operational costs. This clogging of filters is a major challenge, especially when the particles being filtered are soft and squishy, like tiny gels or biological cells, because they can deform and compact to create a dense, impermeable layer.

This research explores how to design better microfilters to prevent this kind of clogging. Instead of a simple mesh, modern microfilters can be designed with an intricate micropillar arrays. The way these pillars are arranged, their size, the space between them, and how densely they are packed can dramatically change how fluid flows through the filter.

Using powerful computer simulations, this study investigated how water flows through different arrangements of these micropillars. We discovered that the filter's design has a significant impact on its performance. For instance, larger pillars and gaps between them allow water to flow more easily.

More importantly, we found that the filter's permeability, a measure of how easily fluid can pass through, is not a fixed value. When we increased the pressure, the permeability went down. This is because the complex paths the water takes around the pillars create eddies in the flow. These eddies create low-flow zones where soft particles are more likely to settle and accumulate, which can lead to clogging.

By understanding how the filter's microscopic geometry creates these flow patterns, we can start to design smarter filters and devices that guide particles through smoothly, minimizing the dead zones where they can get trapped. This research provides a blueprint for developing the next generation of filtration systems that are more effective and resistant to fouling.

Summary

Membrane fouling, particularly by soft, deformable particles, is a significant challenge in microfiltration (MF) processes, leading to reduced efficiency and increased operational costs. This thesis investigates the formation of filter cake layers by numerically simulating fluid flow through microfluidic membranes designed with random, non-overlapping cylindrical micropillar arrays. The study aims to understand how geometric parameters of the porous structure, specifically pillar diameter, minimum pore throat size, and porosity, influence the hydrodynamic properties of the membrane. Using a custom Python-based Monte Carlo (MC) algorithm, 27 distinct 2D micropillar configurations were generated. Computational Fluid Dynamics (CFD) simulations were then performed using COMSOL Multiphysics to solve the steady-state Navier-Stokes equations for water flow. The permeability of each configuration was calculated using Darcy's law, and the results were analysed as a function of pillar geometry and applied inlet pressure (10-40 mbar). The study also includes the fabrication of corresponding physical molds and polydimethylsiloxane (PDMS) microfluidic devices via 3D printing and soft lithography, laying the groundwork for future experimental validation. The simulation results demonstrate that permeability is strongly dependent on the microstructural geometry, increasing with larger pillar diameters, pore throat sizes, and higher porosity, with an increase in porosity of just 0.1 resulting in a more than two-fold increase in permeability. A key finding is the pressure-dependent nature of permeability; in all configurations, permeability decreased near-linearly with increasing inlet pressure. This deviation from classical Darcy's Law indicates the onset of non-Darcian flow, where inertial effects become significant even at low Reynolds numbers ($Re < 10$).

Analysis of the velocity and pressure fields revealed that the disordered pillar arrangements create highly tortuous flow paths, leading to channelling and the formation of eddies in the wake of pillars. These recirculating zones increase the local residence time of particles, raising the likelihood of their adhesion to pillar surfaces, which can initiate fouling. The study concludes that the overall flow resistance and fouling potential are governed by the global pillar network structure rather than solely by localized constrictions. Direct numerical simulation (DNS) proves to be an essential tool for accurately predicting flow behaviour in such complex geometries, as established theoretical models showed significant discrepancies. These findings provide critical insights for optimizing membrane design to minimize fouling by soft particles.

Keywords: Porous Media, Permeability, Micropillar Array, Microfluidics, Membrane Fouling, Soft Particles, Cake Filtration, CFD.

List Of Abbreviations

2D	Two-dimensional
CAD	Computer-aided design
CFD	Computational fluid dynamics
CP	Concentration polarisation
DNS	Direct numerical simulation
KC	Kozeny-Carman
MC	Monte Carlo
MF	Microfiltration
Micro-PIV	Micro-Particle Image Velocimetry
PDMS	Polydimethylsiloxane
PNM	Pore-network models
SLA	Stereolithography

Table Of Contents

1 Introduction

Filtration processes serve as an essential stage widely employed across various industrial sectors including water, chemical, pharmaceutical, and food applications to separate particles and colloids from fluids. Membrane technology plays a vital role in food processing, particularly in protein separation within the dairy sector (Lipnizki et al., 2023). However, its effectiveness is frequently limited by membrane fouling. This phenomenon is defined by the reduction of filtration performance due to particle accumulation on membrane surfaces or within its pores, especially during filtration of deformable or soft particles (Rudolph et al., 2019).

While the behavior of rigid particles during filtration is generally well understood, the filtration of soft, deformable particles such as microgels, emulsions, and biological cells presents additional challenges due to their complex mechanical properties. These particles have the capability of changing shape, reorganizing and compressing under pressure, which directly affects the structure of the resulting filter cake (Schroën & Bouhid de Aguiar, 2023).

In cake filtration, particles gradually deposit on the filter surface to form a porous cake layer. The physical characteristics of this cake are influenced not only by particle size but also by their flexibility and interaction with the filter material. In the case of soft particles, deformation can lead to the formation of denser, less permeable cakes, increasing flow resistance (Schroën & Bouhid de Aguiar, 2024).

Cake layers can become highly compressed, leading to a significant decrease in water flux. In severe cases, this compression can eliminate voids within the cake, effectively blocking the flow and bringing the water flux to near zero. This phenomenon poses a substantial hydrodynamic resistance to the overall filtration process, reducing its efficiency and increasing energy demands (Lüken et al., 2021; Stüwe et al., 2024). For soft particles, the conventional understanding that pore size dictates membrane performance is insufficient, as their deformability can lead to irreversible compression with severe consequences (Bouhid de Aguiar et al., 2019).

Predicting particle pathways and understanding the flow path of water in porous media is crucial for investigating cake layer formation due to soft particles. In porous media, streamlines can exhibit non-trivial trajectories (De Winter et al., 2021). Streamlines are observed with velocity fluctuations and indicate changes in flow direction, which can significantly impact particle transport and deposition. Particle tracking helps distinguish between reversible and irreversible compression events in the cake, which directly impacts the permeability and resistance of the filter cake over time (Lüken et al., 2021).

Recent advancements in microfluidics and microfabrication techniques have facilitated the development of microfluidic models that accurately mimic porous media, particularly through the integration of micropillar arrays (Wang & Wang, 2017). These micropillar arrays serve as simplified, yet highly representative, analogues of natural porous structures, enabling precise control over geometric parameters such as pillar diameter, spacing, and height, which are crucial for fundamental investigations (Goswami et al., 2025). Such systems are particularly relevant for applications like high-performance liquid chromatography, microreactors, micro-filters, and heat pipes, where understanding and optimizing fluid flow are paramount (Gräfner et al., 2022; Hale et al., 2014b, 2014a; Hulikal Chakrapani et al., 2022; Zhou et al., 2016).

While experimental characterization of porous media properties at small scales presents inherent difficulties, numerical simulations offer a robust and accurate means to delve into pore-scale phenomena, providing insights often unattainable through solely empirical methods (Hale et al., 2014b; Nie et al., 2024).

This thesis specifically focuses on the numerical simulation of flow within microfluidic membranes incorporating random cylindrical micropillar arrays. Disordered arrangements, while more complex to model than regular ones, often more accurately represent the heterogeneity found in real porous materials. The inherent complexity of random distributions significantly impacts fluid behavior, leading to challenges in predicting macroscopic transport properties such as permeability (Yazdchi et al., 2011, 2012). Key geometrical parameters of these micropillar arrays, including pillar size/diameter, pore throat dimensions, and overall porosity, critically influence the flow characteristics and, consequently, the permeability (Mohammadi & Riazi, 2022; Nie et al., 2024; Tamayol et al., 2012).

Given these intricate dynamics, a detailed understanding of flow in porous media during filtration is essential to minimize membrane fouling and the decrease in water flux due to cake formation. Therefore, ongoing research in this area is critical for many applications and industries to develop filtration systems that are capable of handling soft particles effectively.

1.1 Aim

The primary objective of this study is to investigate the hydrodynamic properties of microfluidic membranes featuring disordered micropillar arrays and to understand how these properties relate to membrane fouling by soft particles. This study seeks to systematically determine the influence of key geometric parameters, specifically pillar diameter, minimum pore throat size, and porosity on the permeability and flow behavior within these micro-structured porous media. Through detailed CFD simulations, the research aims to characterize the velocity and pressure fields, identify the onset of non-Darcian flow, and analyze the formation of flow patterns, such as channeling and eddies, that contribute to fouling initiation. Ultimately, the goal is to provide fundamental insights that can guide the design of more efficient and fouling-resistant MF membranes.

2 Background

2.1 Membrane for Food Applications

Membrane technology has gained considerable interest within the food industry, evolving from niche process to a pivotal unit operation in diverse arrays of the food and beverage production processes (Lipnizki & Dupuy, 2013). This widespread adoption stems from several key advantages over conventional separation methods, notably its relatively low energy consumption and ability to selectively separate components without requiring heat or additives (Lipnizki & Dupuy, 2013; Schroën & Bouhid de Aguiar, 2023). Consequently, membrane filtration is also extensively utilised across various sectors, including water and wastewater treatment, and biotechnology (Chew et al., 2020; Cirillo et al., 2023; Lüken et al., 2020; Valencia et al., 2022).

The spectrum of membrane processes employed, includes MF, ultrafiltration (UF), nanofiltration (NF), and reverse osmosis (RO), each tailored to specific separation requirements based on pore size or molecular weight cut-off (Cirillo et al., 2023; Lipnizki & Dupuy, 2013; Schroën & Bouhid de Aguiar, 2024). For instance, UF is for protein concentration, such as in milk preconcentration and whey protein concentration in the dairy industry (Cirillo et al., 2023; Lipnizki et al., 2023). Conversely, MF is commonly deployed for retaining larger components like cells, cell debris, bacteria, and particulates, finding application in potable water production, as well as in the wine and vinegar industries (Cirillo et al., 2023). Beyond these, emerging processes such as vapour permeation (VP) and pervaporation (PV) are also gaining action, particularly in biorefineries for the pre-concentration and concentration of biofuels and biochemicals (Lipnizki et al., 2019).

Despite the demonstrable efficacy and broad applicability of membrane processes, a formidable challenge persists: membrane fouling (Chew et al., 2020; Cirillo et al., 2023; de Aguiar & Schroën, 2020a; Lipnizki & Dupuy, 2013). This phenomenon, characterised by the deposition of unwanted matter on the membrane surface or within its pores, invariably leads to a reduction in permeate flux and overall process efficiency (Ben Hassan et al., 2014; Chew et al., 2020; Cirillo et al., 2023; Lipnizki & Dupuy, 2013; Lüken et al., 2020; Ngene et al., 2011; Valencia et al., 2022). Fouling mechanisms are multifaceted, encompassing concentration polarisation (CP), external cake layer formation, internal pore blocking, and adsorption of foulants (Chew et al., 2020; Cirillo et al., 2021; de Aguiar & Schroën, 2020a; Giiell & Davis, 1996; Rudolph et al., 2019). These issues can be reversible, allowing removal by rinsing, or irreversible, necessitating more rigorous chemical cleaning (Rudolph et al., 2019). The complex nature of bio-based feed streams, often comprising macromolecules, organic colloids, and microorganisms, further exacerbates fouling challenges in the biotechnology, biorefinery, and food sectors (Rudolph et al., 2019). Traditional approaches to mitigating fouling include operating below the critical or at the sustainable flux, although this may necessitate larger membrane areas and plant sizes to maintain productivity (Lipnizki & Dupuy, 2013). More actively, cleaning methods such as backflushing are widely applied in industrial settings (Lüken et al., 2020).

2.2 Microfluidics

To gain a deeper understanding of these microscopic fouling phenomena and ultimately to optimise membrane processes, researchers are increasingly turning to microfluidic devices as powerful analytical tools (de Aguiar & Schroën, 2020a; Linkhorst et al., 2016; Schroën et al., 2020). These miniaturised platforms offer unparalleled capabilities for real-time observation

and detailed analysis of filtration processes at scales ranging from nanometres to millimetres (de Aguiar & Schroën, 2020a). Microfluidic chips allow for the direct visual characterisation of membrane fouling and particle deposition on membrane surfaces (Ngene et al., 2010). For instance, a microfluidic system can effectively retain filtered particles at a membrane-mimicking structure, providing a visual cross-section of the developing filter cake (Lüken, 2022). This direct observation permits the monitoring of cake thickness and particle trajectories, alongside pressure and flux data (Ngene et al., 2010). Such detailed insights are crucial for understanding particle-pore interactions, which are often obscured in macroscopic membrane systems (Linkhorst et al., 2016).

The design of microfluidic devices for studying porous media and filtration is highly versatile. These devices frequently incorporate arrays of micropillars or cylinders to mimic the intricate pore structures found in real membranes (Goswami et al., 2025; Jahanbakhsh et al., 2020; Wang & Wang, 2017). The geometry of these pillar arrays, defined by parameters such as diameter, height, and inter-pillar distances, significantly influences fluid flow and permeability (Hale et al., 2014b, 2014a; Tamayol et al., 2012). Experiments often involve injecting fluids like water or hexadecane through these pillared microstructures and measuring effective permeabilities based on Darcy's law, noting that these permeabilities typically remain independent of the fluid used (Hulikal Chakrapani et al., 2022). Researchers utilise techniques such as micro-Particle Image Velocimetry (micro-PIV) to measure velocity fields and pressure differences within porous chips, enabling a more accurate understanding of permeability distribution (Jahanbakhsh et al., 2020; Wang & Wang, 2017). Studies have shown that permeability often aligns with classical models such as the Kozeny–Carman equation (Wang & Wang, 2017). Furthermore, microfluidic devices facilitate the investigation of phenomena like CP, which can be minimised by optimising feed channel height (Kaufman et al., 2012).

The fabrication of these sophisticated microfluidic devices commonly involves materials such as polydimethylsiloxane (PDMS), silicon, and glass (Anbari et al., 2018; Debnath & Sadrzadeh, 2018; Fallahi et al., 2019; Gerami et al., 2016; Massimiani et al., 2023). PDMS is favoured due to its transparency, flexibility, biocompatibility, and ease of fabrication through soft lithography (Ferreira et al., 2024; Kaufman et al., 2012; Lin & Chung, 2021; Tamayol et al., 2012). However, its inherent hydrophobicity and subsequent hydrophobic recovery after surface treatments pose challenges for self-driven capillary microchips, necessitating effective hydrophilicity treatments such as polyethylene glycol (PEG) coating (Lin & Chung, 2021). Paper-based analytical devices (PADs) represent another significant advancement, offering affordable, user-friendly, and equipment-free solutions for point-of-care (POC) diagnostics in various sectors, including health, environment, food, and energy (Anushka et al., 2023). These paper-based systems often leverage capillary forces for fluid flow, eliminating the need for external pumps (Anushka et al., 2023).

Beyond simple fluid flow, microfluidics enables the study of complex interactions relevant to food processing. This includes the transport of soft colloids, vesicles, and deformable particles like cells and immiscible droplets through porous media, which is pertinent to filtration in food, water, and life sciences (Benet et al., 2017). For instance, microfluidic approaches have provided insights into early film formation in protein-stabilised emulsions, confirming that convective mass transport often dominates over diffusion in such systems (Hinderink et al., 2021). The application of microfluidic spinning technology (MST) allows for the production of microfibers and nanofilms with controlled sizes and morphologies, holding potential for encapsulating sensitive components and improving food packaging (Mu et al., 2022). Moreover,

microfluidics have been explored for optimising emulsification processes, with designs ranging from T- and Y-junctions to flow-focusing devices, enabling the controlled formation of monodisperse emulsion droplets (He et al., 2020; Schroën et al., 2020). This level of control, alongside the ability to study interfacial properties and coalescence stability at short timescales, provides invaluable data for industrial emulsification (Muijlwijk et al., 2016).

The insights gained from microfluidic investigations are critical for advancing membrane technology towards more sustainable and efficient food processing. By elucidating the fundamental mechanisms of particle behaviour, filter cake formation, and fluid dynamics at the microscale, these tools facilitate the design of innovative membrane architectures and processing conditions that can minimise fouling, reduce energy consumption, and ultimately contribute to a more sustainable circular economy in food production (de Aguiar & Schroën, 2020b; Linkhorst et al., 2016; Schroën et al., 2020; Schroën & Bouhid de Aguiar, 2023). The integration of these microscale findings with macroscopic process design holds the potential to transform current industrial practices, leading to better-defined products and enhanced resource utilisation (Schroën et al., 2020).

2.3 Fluid Flow in Porous Microstructure Media

2.3.1 Permeability in Porous Media

Fluid transport within porous media is inherently multiscale, necessitating analysis from macroscopic to microscopic pore levels to accurately predict large-scale phenomena (Karimifard et al., 2021). However, the experimental characterisation of permeability, particularly at the microscale, presents several formidable challenges. A primary difficulty arises from the porous medium's inherent heterogeneity and potential microstructural alterations during sampling and experimentation, such as dynamic changes in pore morphology due to mineral dissolution or biofilm growth (Karimifard et al., 2021; Musabbir Rahman et al., 2025). Furthermore, practical issues like pressure inconsistencies and wall effects frequently complicate microchannel flow measurements, especially as non-uniform porosity near boundaries can substantially influence results at higher flow rates (Karimifard et al., 2021; Rahmanian et al., 2023). Lastly, the complex nature of porous media, often featuring irregularly shaped or nanoscale pores, as seen in unconventional reservoirs, introduces significant measurement complexities where conventional models like Darcy's law may no longer apply, necessitating the consideration of alternative flow mechanisms such as slippage (Cao et al., 2016; Karimifard et al., 2021; Xia et al., 2017).

Recent scholarly endeavors have further advanced the understanding of permeability in microfluidic systems. Chakrapani et al. (2023), for instance, extensively investigated the permeability of pillar arrays within microfluidic devices, applying Brinkman’s theory to account for wall friction effects. Their work encompassed both experimental measurements and simulations, providing effective permeabilities for various pillar arrangements across a broad range of porosities (0.58, 0.65, 0.73 and 0.87). These studies compared simulation data for square, rotated square, and hexagonal pillar lattices with several established theoretical expressions, demonstrating good agreement across different porosity regimes. Furthermore, the investigation extended to disordered pillar configurations, with their findings aligning with predictions from models such as that by Yazdchi et al. (2011) for irregular pillar arrays. For a comprehensive overview of theoretical permeabilities pertinent to irregular configurations in two-dimensional (2D) systems, Table 2.1, adopted from Chakrapani et al. (2023), provides a structured summary.

Concurrently, Nie et al. (2023) contributed significantly to the characterization of permeability in structured porous media through combined experimental and numerical approaches utilizing microfluidic models. Their research primarily focused on comparing observed permeabilities with predictions from the Kozeny-Carman (KC) equation, noting that the classic KC equation only roughly agrees with experimental results when porosity is between 0.50 and 0.60, and fails outside this range. They observed that permeability decreases with increasing Reynolds number beyond a threshold of Re=1, and generally increases with micropillar diameter. Additionally, Nie et al. (2023) found that a triangular pillar arrangement yielded lower permeability and higher tortuosity compared to a square arrangement, and they proposed a tortuosity model for quasi-2D microfluidic models.

Table 2.1. Theoretical permeabilities of irregular distributions in 2D. Adopted from (Chakrapani 2023).

Author(s)	Abbrev.	Permeability
(Koch & Ladd, 1997)	KL	$\frac{\sqrt{2}}{17}\frac{\varepsilon_c^{5/2}}{\phi}$, for $\varepsilon < 0.6$ $\frac{2.76}{\phi \exp(11.1\phi)}$
(Yazdchi et al., 2011)	YSL	$0.2d^2\chi(\gamma_2){\gamma_2}^{5/2}$, with $\gamma_2 = 0.26\phi^{0.6790} - 0.47$ and $\chi(\gamma_2) = 1 - 0.5e^{-3.0\gamma_2}$

2.3.2 Numerical Simulation Methods in Porous Media Analysis

To address these limitations, numerical simulation has emerged as a valuable approach for estimating permeability and examining both fluid dynamics and the underlying pore architecture in three dimensions. A prerequisite for simulating flow directly within 3D porous geometries is an accurate morphological representation of the medium under investigation.

In recent years, the flow behaviour of non-Newtonian fluids has gained increasing attention due to their relevance in various scientific and industrial fields such as geoscience, biomedicine, and enhanced oil recovery (Johnston et al., 2004; Choi, 2009; Suleimanov et al., 2011; Mader et al., 2013). Nanofluids, containing particles on the nanometer scale, have demonstrated improved oil recovery efficiency (Wasan and Nikolov, 2003; Huang et al., 2013). Similarly, the rheological behaviour of magmas, and hence their eruption dynamics, is governed by the volume and distribution of bubbles and crystals (Mader et al., 2013; Cassidy et al., 2018). In systems where suspended particles are significantly smaller than the domain size, the bulk behaviour is typically described by an effective rheology, which often deviates from Newtonian assumptions. The precise physical mechanisms underlying the non-Newtonian behavior in

magma remain uncertain (Deubelbeiss et al., 2011). Such behaviour is generally linked to interactions among suspended particles and between particles and fluid. This underscores the necessity of developing numerical models capable of representing non-Newtonian fluid flow through porous networks.

2.3.3 Flow Regimes in Porous Media

Flow behaviour in porous media is frequently described by the Reynolds number, which compares inertial and viscous forces. Due to the tiny pore sizes, flow in porous media generally occurs at very low Reynolds numbers, exhibiting laminar characteristics. For example, typical Reynolds numbers range from extremely low values in magmatic systems (Glazner, 2014) to slightly higher values in groundwater flow.

Under these low-Reynolds conditions, the incompressible Navier–Stokes equations simplify to the Stokes equations, which neglect gravitational effects. When the internal structure of the porous medium is known, these equations enable direct simulation of laminar flow within it. However, such detailed modelling becomes computationally unfeasible at larger scales.

For Newtonian fluids, an effective permeability is often introduced, linking flow rate, pressure gradient, and viscosity via Darcy's law (Andrä et al., 2013b; Saxena et al., 2017; Bosl et al., 1998). This relation forms the fundamental basis for upscaling flow behaviour in homogeneous porous systems.

Darcy's empirical law remains the standard tool to describe laminar, single-phase flow in homogeneous porous media (Costa et al., 1999). However, it neglects inertial forces, which become relevant at higher Reynolds numbers. To address this, Forchheimer introduced a modified expression that incorporates nonlinear inertial effects (Macini, Mesini, and Viola, 2011).

2.3.4 Porosity–Permeability Relationships and Advances in Pore-Scale Modeling

While permeability may be derived through experimental methods across various scales, advances in computational modelling have enabled predictions of large-scale subsurface flow using pore-scale permeability data as input. Consequently, accurate determination of pore-scale permeability is essential.

One commonly employed method links porosity with permeability. Nevertheless, defining this relationship precisely has proven challenging and has been the subject of extensive study (Kozeny, 1927; Carman, 1937, 1956; Mavko and Nur, 1997). Although porosity is a significant factor, permeability also strongly depends on the geometrical complexity of the pore space. Hence, traditional porosity-permeability models remain limited in accuracy.

The emergence of pore-scale modelling techniques, supported by imaging methods such as X-ray computed tomography, has allowed researchers to examine fluid flow at the microstructural level. These simulations yield detailed spatial distributions of velocity and pressure under imposed pressure gradients, enabling more refined estimates of permeability.

The simulation of immiscible fluid interactions at the pore scale has evolved significantly alongside improvements in imaging and computational tools. Modern pore-scale modelling aims to resolve complex multiphase flow within porous materials, particularly at the level where

fluid interfaces interact. A variety of numerical approaches have been developed for this purpose, including pore-network models (PNM), lattice–Boltzmann methods (LBM), and particle-based techniques like dissipative particle dynamics (DPD) and smoothed particle hydrodynamics (SPH). Other frameworks include DNS, mesh-free Lagrangian approaches, and grid-based CFD with capabilities for interface tracking and dynamic contact angle modelling (Liu et al., 2013).

These modelling approaches generally fall into two categories: direct methods that solve governing equations (e.g., Navier–Stokes or Boltzmann) within detailed pore geometries, and simplified PNM that approximate the medium as a system of connected pore bodies and throats using rules such as Poiseuille's law (Graveleau et al., 2017). PNM techniques provide computationally efficient tools for analysing multiphase transport and have been widely used to extract flow and pressure distributions at the microscale (Hassanizadeh, 2002). For instance, Hughes and Blunt (2000) used such models to examine how contact angle and flow rate influence imbibition behaviour.

Despite their utility, PNM approaches are limited by the geometric and physical assumptions they require. Direct or grid-based simulations offer greater numerical accuracy, particularly in scenarios with large density and viscosity contrasts, making them the preferred method when high-fidelity fluid behaviour is needed.

Recent work has focused on extending Darcy's law through various theoretical frameworks, including effective medium theory (Sahimi and Yortsos, 1990), pore network models (Shah and Yortsos, 1995), and numerical simulations at the pore scale (Aharonov and Rothman, 1993; Vakilha and Manzari, 2008).

Given the challenges associated with experimental measurements of permeability, especially in complex micro/nanoporous media, numerical approaches based on geometrical and structural models—such as the Kozeny–Carman equation and its variants—have become increasingly important. These models relate permeability to measurable parameters like porosity, tortuosity, and specific surface area. Although widely used, the Kozeny–Carman model often falls short when applied to irregular or highly tortuous geometries. Consequently, numerous studies have sought to refine or generalize it by incorporating additional structural characteristics (Chen et al., 2015; Xiao et al., 2012; Khabbazi et al., 2016; Costa, 2006).

The accurate estimation of fluid flow through porous structures demands a multifaceted approach that integrates empirical data, theoretical models, and advanced simulation techniques. Continued efforts to refine porosity-permeability relationships, particularly for non-Newtonian fluids and complex geometries, are crucial for improving our understanding of transport processes in natural and engineered porous systems.

3 Materials and Methods

3.1 2D Pillar Generation

2D non-overlapping disordered circular pillar array configurations were generated using a custom-developed computational approach via Python, Visual Studio Code v1.101.2 (Microsoft, USA) was used for code scripting, editing and executing. The pillar array configurations were developed within a rectangular computational domain measuring 21 mm in length and 7 mm in width (see Figure 3.1). Periodic boundary conditions were imposed along the y-axis to replicate a repeating geometry in the transverse direction, while the boundaries of the x-axis remained fixed, reflecting the physical constraints of inlet and outlet present in typical microfluidic applications.

Initially, a random placement (RP) algorithm was explored for distributing the circular pillars within the preset domain in which circular pillars were inserted one at a time at randomly selected coordinates within the domain. Any proposed location that resulted in overlap with an existing pillar was rejected, and the algorithm continued until no further placements could be made. While this approach offered straightforward means of generating non-overlapping structures, it proved inadequate for achieving the desired porosities. As the packing density increased, the system tended toward a jammed state, which agrees with (Yazdchi et al., 2012). This limitation became particularly evident when targeting lower porosity values (below approximately 0.6 in our case), where the RP approach failed to converge reliably. Consequently, a more robust approach was necessary to ensure the precise and random arrangement of pillars according to the specified design parameters.

To address the limitations of the initial approach, a MC algorithm was adopted to enable greater control over both randomness and porosity. The MC simulation was initiated by populating the rectangular domain with a uniformly spaced grid of circular pillars. Excess pillars were randomly removed until the number remaining corresponded to the target porosity for a given pillar size and pore throat. Subsequently, the core of the MC approach involved an iterative process of randomly perturbing the spatial position of each of the remaining pillars. For each configuration, the simulation was executed for a total of 10^6 perturbation steps to achieve sufficient spatial decorrelation and ensure a thoroughly randomized and statistically decorrelated arrangement. During each step, the displacement of a randomly selected pillar was accepted only if the proposed move preserved the non-overlapping condition and maintained the minimum spacing between pillars, enforcing the defined pore throat size.

Pillars were represented as circular disks with core diameters of either 250 µm, 300 µm, or 350 µm, depending on the configuration. The space between neighboring pillars, referred to as the pore throat, was established by adding a spacing value (either 50, 60, or 70 µm) to the core diameter, a similar approach as Hulikal Chakrapani et al. (2022). This effective outer diameter governed the overlap-checking condition within the simulation. Each configuration was thus uniquely defined by a triplet of parameters: pillar diameter, minimum pore throat, and porosity. For instance, a configuration labelled as (300, 60, 0.6) would correspond to a pillar diameter of 300 µm, a minimum pore throat of 60 µm, and a porosity of 0.6.

A total of 27 distinct configurations were generated by systematically combining three pillar diameters, three spacing values, and three target porosities (0.5, 0.55, and 0.6). For each case, the actual porosity was calculated by subtracting the total projected area of the pillars from the

domain area, then dividing by the domain area. The MC method successfully achieved porosities within ±0.1% of the target for most configurations. However, a few combinations, specifically (250 µm, 60 µm), (250 µm, 70 µm), and (300 µm, 70 µm), could not reach the lowest target porosity of 0.5. These cases instead stabilized at porosities slightly above 0.5 and displayed a more ordered, grid-like arrangement, suggesting spatial constraints limited their ability to form truly disordered structures at high packing densities.

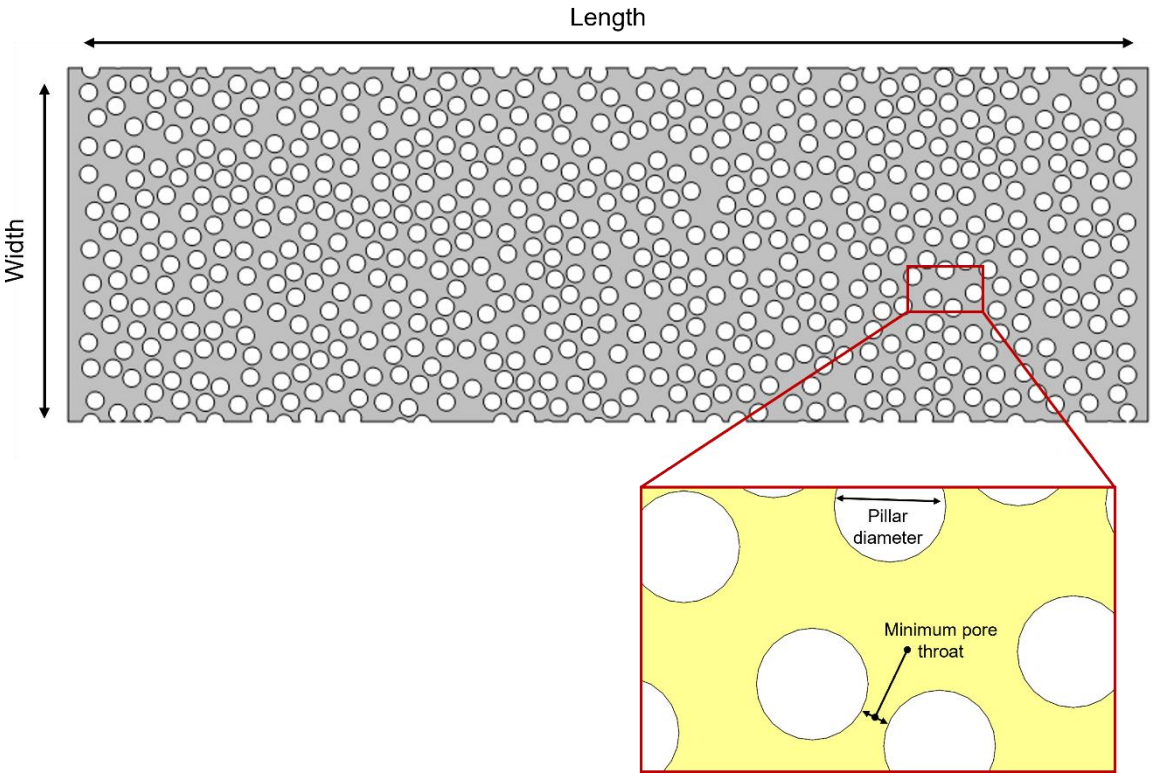

Figure 3.1. Numerical representation of a 2D microfluidic membrane with disordered micropillar configuration, designed using Python and generated using MC simulation. White circles representing micropillars. Flow pathways are shown in grey (extended view) and yellow (magnified view), indicating the minimum pore throat and micropillar diameter.

3.2 Numerical Simulation

In this study, the generated 2D pillar configurations were investigated using CFD to examine how variations in pillar diameter, pillar throat, porosity, and membrane geometry influence fluid transport behavior. All simulations were conducted using the commercially available software platform COMSOL Multiphysics v6.3 (COMSOL Inc., Sweden). The simulations focused on modeling the behavior of water flow within the membrane structure, particularly around the embedded pillars.

To simulate the fluid dynamics, a single-phase laminar flow physics interface (spf) was used to solve the steady-state Navier–Stokes equations for an incompressible fluid. The governing equations, vector equation conservation of momentum and the continuity equation for mass conservation are presented below as Equations (3.1) and (3.2), respectively:

$$\rho(u \cdot \nabla)u = \nabla \cdot [-pI + K] + F \quad \text{(Eq. 3.1)}$$

$$\rho \nabla \cdot u = 0 \quad \text{(Eq. 3.2)}$$

where ρ denotes the fluid density (assumed to be 1000 kg/m³ for water), u represents the velocity factor (m/s) for the 2D simulation in the free flow domain, p is the pressure (Pa), F is the volume force vector (N/m^3), I is the identity matrix, and K is the viscous stress tensor (Pa) defined in Equation (3.3) as:

$$K = \mu(\nabla u + (\nabla u)^T) \quad \text{(Eq. 3.3)}$$

where μ is the dynamic viscosity of water (0.001 Pa·s), and T is the absolute temperature (K).

The Reynolds number was found to be between 1 and 10 for the different pillar configurations which is consistent with the applicability of Darcy's law that holds for an upper limit Reynolds number value between 1–10 (Wang et al., 2019). A constant pressure boundary condition was applied to the inlet and the outlet of the domain. An inlet pressure of 10 mbar was set, while the outlet pressure was set to 0. A no-slip boundary condition was applied to the pillar surfaces and walls of the membrane. To study the effect of changing the inlet pressure on the membrane permeability, a parametric sweep was applied with inlet pressures of 10, 20, 30, and 40 mbar.

For all studied pillar configurations, the computational domain was discretized using a physics-controlled mesh with finer element sizes which resulted in approximately 220,000 to 250,000 mesh elements, including both domain and boundary elements. Following the simulations, pressure distribution and velocity profiles of the water flow through the membrane structure were evaluated and visualized.

The permeability of the porous membrane was determined using Darcy's law as shown in Equation (3.4)

$$k = \frac{Q\ \mu\ L}{A\ \Delta P} = \frac{u_D\ \mu\ L}{\Delta P} \quad \text{(Eq. 3.4)}$$

where k is the effective permeability of the membrane (m^2), Q denotes the volumetric flow rate through the membrane (m^3/s), L is the length of the membrane (m), ΔP is the pressure drop between the inlet and the outlet domains, A is the membrane cross-sectional area (m^2), and u_D is the Darcy velocity (m/s).

In addition, the intrinsic permeability of the membrane domain (k_i) was estimated using the KC Equation (3.5):

$$k_i = \frac{d^2\,\varepsilon^3}{180\,(1-\varepsilon)^2} \qquad \text{(Eq. 3.5)}$$

where d denotes the pillar diameter and ε represents the porosity of the membrane structure.

3.3 3D-printed Mold Preparation

The Python-based 2D pillar configurations were saved in Drawing Exchange Format (.dxf), which are then imported and incorporated into the overall 3D mold design. All molds were designed using computer-aided design (CAD) software, specifically SolidWorks 2025 SP2.0 (Dassault Systèmes, France), as illustrated in Figure 3.2a. To promote homogeneous flow conditions within the microfluidic device, a filleted-top triangular inlet geometry was incorporated into the chip design. The overall chip height was set to 400 μm as a fixed structural parameter. The 3D designs were saved in stereolithography (SLA) format (.stl) and directly imported into the 3D printer software PreForm 3.49.0 (Formlabs, USA) for 3D printing preparation. A Form 3+ SLA 3D printer (Formlabs, USA) was used to fabricate the mold parts. The digital models were processed using the PreForm software, which segmented them into successive thin layers for printing. Fabrication was carried out through a layer-by-layer photopolymerization of Clear Resin v4 (Formlabs, USA) using a focused laser source.

Following completion of the printing cycle, the molds were retained on the build platform to allow any excess resin to settle. Subsequently, they were immersed in into a 100% isopropanol solution using the Form Wash FH-WA-01 (Formlabs, USA) and washed for 20 minutes to remove uncured resin. Once cleaned, the molds were carefully detached from the build platform and air blow gun was used to ensure complete evaporation of residual isopropanol. Subsequently, the printed molds underwent a post-curing process using the Form Cure FH-CU-01 (Formlabs, USA), where the temperature was gradually increased from room temperature (23 °C) to 60 °C. Once the desired temperature was reached, the molds were cured under 405 nm UV light for 15 minutes. This post-curing procedure is essential, as it enhances the physical and mechanical performance of the printed molds by reinforcing material properties post-fabrication. After post-curing, molds were visually inspected under a microscope to assess the quality of fine structural features, including the fidelity of the micropillars. Molds were uniformly sprayed with Citadel paint spray (Citadel Miniatures, UK) (see Figure 3.2b-d). This step was carried out to facilitate demolding during the subsequent soft lithography process by preventing the adhesion of PDMS to the mold surfaces during the replication.

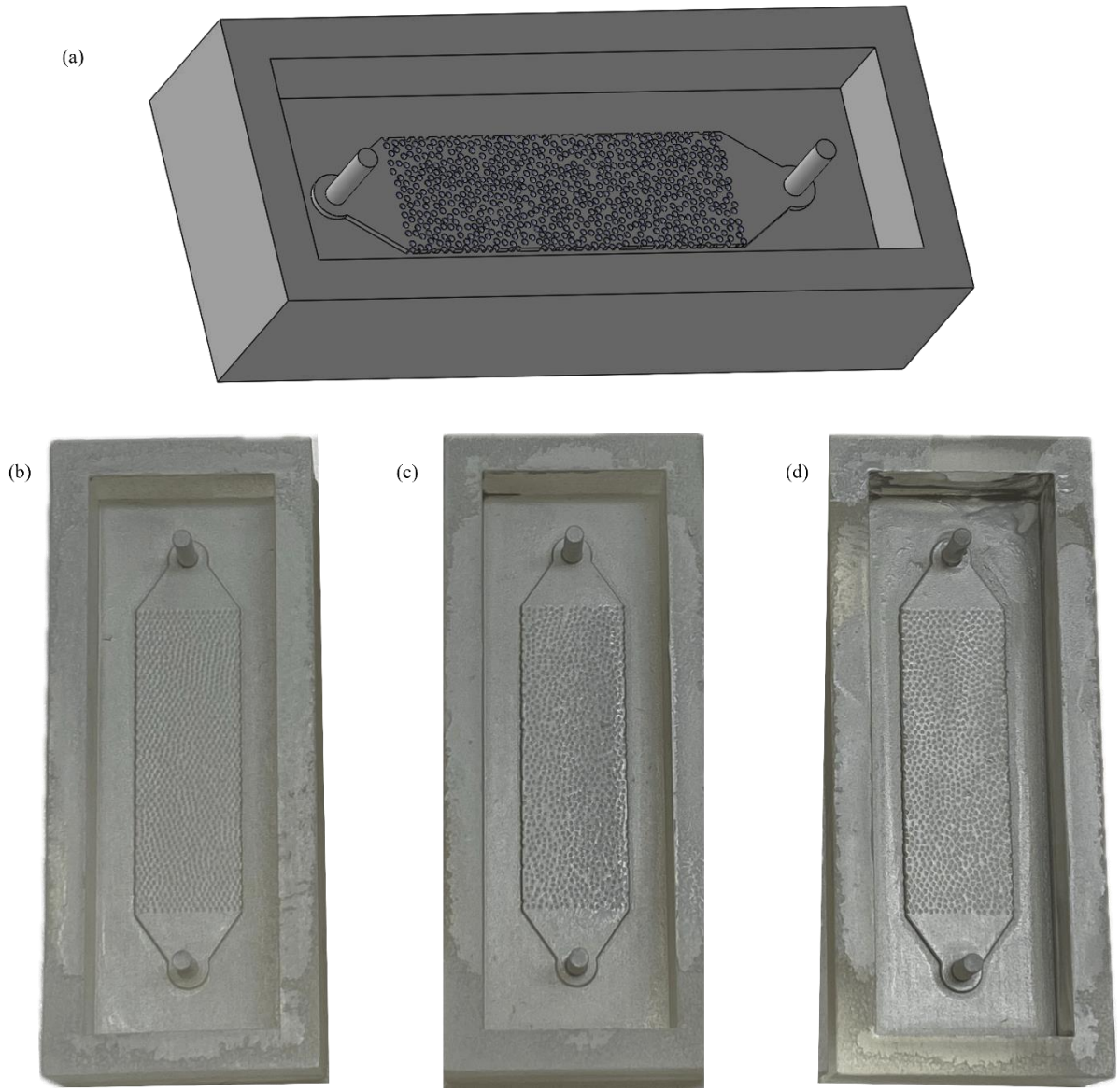

Figure 3.2. 3D-printed mold design and fabrication. CAD model of the mold with a pillar size of 350 μm and porosity of 0.6. (b-d) Top-view of the 3D-printed molds after post-curing and spray-coating with a pillar size of 300 μm and porosities of 0.5, 0.55, and 0.6, respectively. All designs have a 60 μm pore throat and 400 μm height.

3.4 PDMS Microfluidic Membrane Fabrication

PDMS microfluidic membranes shown schematically in Figure 3.3 were fabricated using RTV 615 A, a silicone base casting resin, and RTV 615 B, a curing agent (Permacol B.V., Netherlands). Two different PDMS blends were prepared to serve distinct functional layers in the microfluidic chip: one rich in curing agent (referred to as B-rich) and the other rich in base polymer (referred to as A-rich). For the B-rich solution, RTV 615 A and RTV 615 B were added in a 4:1 weight ratio. The components were stirred in a disposable paper cup until a uniform mixture was achieved. To remove any air bubbles introduced during mixing, the solution was

degassed in a vacuum desiccator for approximately 30 minutes. Following this, the degassed mixture was poured into a mold designed to form the microfluidic pillar array features (see Figure 3.4b). In parallel, the A-rich PDMS solution was prepared by mixing RTV 615 A and B in a 30:1 ratio. As with the B-rich mixture, thorough mixing was followed by vacuum degassing for 30 minutes. This blend was poured into a separate mold to create the base layer of the chip (Figure 3.4a).

Once both molds had been filled, they underwent a secondary degassing process lasting approximately one hour to further remove trapped air. After degassing, the molds were transferred into a preheated oven set at 80 °C. The samples were thermally cured for 45 minutes, with the first 5 minutes allowed for temperature stabilization and the remaining 40 minutes for full polymerization. Upon removal from the oven, the mold containing the microfluidic features was cooled in a refrigerator for 10 minutes to aid demolding. The structured PDMS layer was then gently peeled from the mold and aligned onto the pre-cured base layer. This assembly was placed back in the oven at 80 °C and left to cure overnight, allowing for irreversible bonding through thermal crosslinking. After the overnight bonding process, the fully assembled chip was removed from the oven and stored in a refrigerator for an additional 2 to 3 hours to promote mechanical stability. Finally, the fabricated microfluidic membrane was carefully cut from the mold using a sharp blade for subsequent experiments as shown in Figure 3.4c and d.

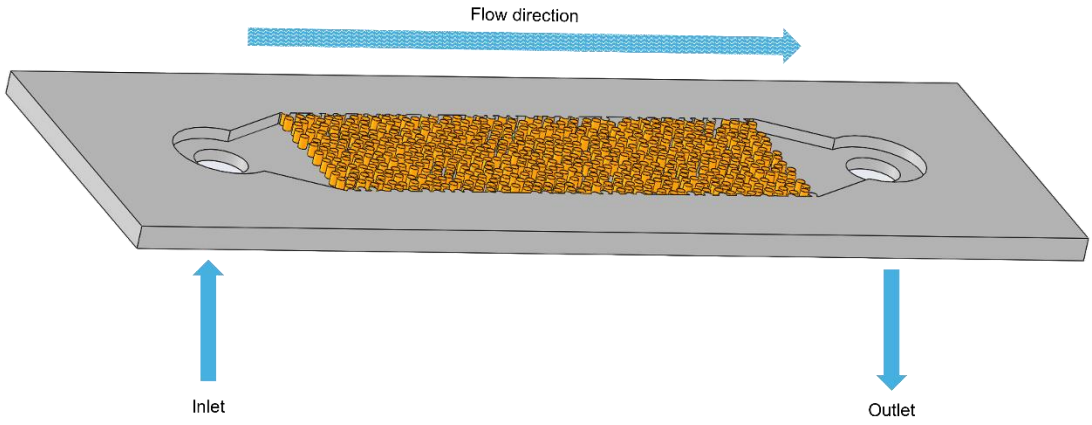

Figure 3.3. A 3D schematic of the microfluidic device. Blue arrows indicate the overall flow direction from the inlet to the outlet, passing through the porous medium composed of a disordered micropillar array (orange).

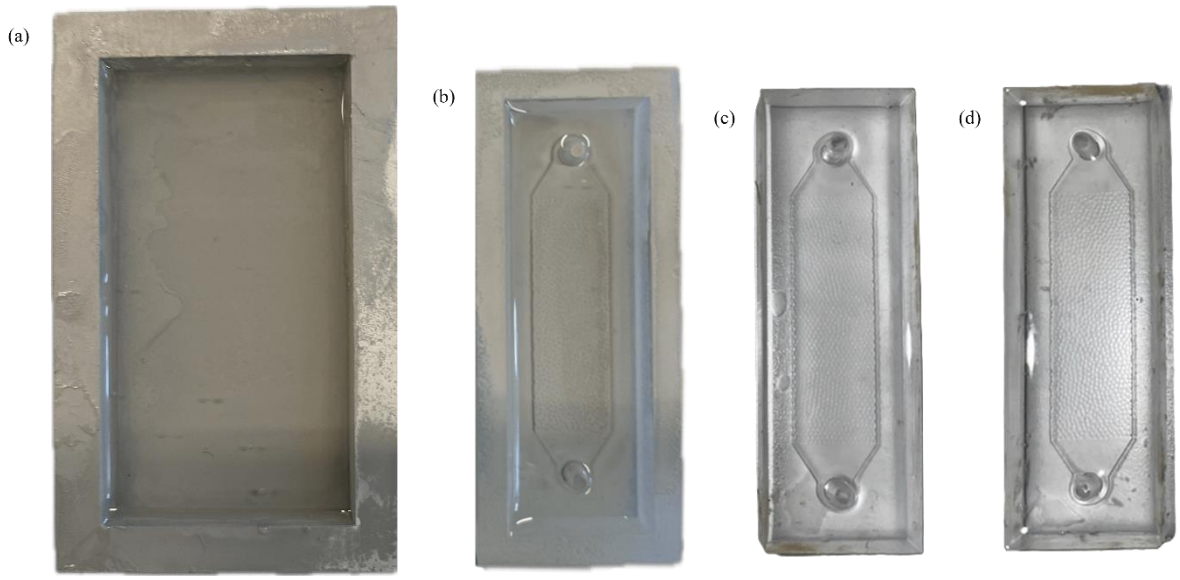

Figure 3.4. Top-view of the PDMS microfluidic chip fabrication process. (a) Base mold containing the A-rich PDMS solution. (b) Feature mold containing the B-rich PDMS solution. (c, d) Final, bonded PDMS microfluidic chips after demolding with a pillar size of 300µm, a pore throat of 60µm, and a height of 400µm, with porosities of 0.5 (c) and 0.55 (d).

4 Results and Discussion

This section presents and discusses the numerically simulated hydrodynamic properties of the disordered micropillar arrays. The analysis is structured to first outline the influence of pillar size, pore throat size, and porosity on the intrinsic permeability. Subsequently, it examines the effect of operational pressure, revealing significant deviations from classical Darcian flow. These findings are then critically evaluated against established theoretical models, and their implications for the broader research objective of understanding soft particle filtration are explored.

4.1 Effect of Pillar Size on Permeability

The effect of pillar size on permeability was systematically explored through numerical simulations using disordered arrays of circular micropillars with diameters of 250, 300, and 350 µm. The analysis was conducted across three porosities of 0.5, 0.55, and 0.6 and under inlet pressures of 10, 20, 30, and 40 mbar, while maintaining a minimum pore throat of 50 µm. The results for each porosity scenario are presented in Figures 4.1, 4.2, and 4.3.

At a fixed porosity of 0.50, Figure 4.1 illustrates a clear relationship between pillar diameter, pressure, and permeability. A steady decline in permeability was observed for all pillar sizes with increasing inlet pressure from 10 to 40 mbar. The 250 µm pillars configuration exhibited the lowest permeability, which reduced by approximately 4.9% as pressure increased from 10 to 40 mbar. Meanwhile, the 300 µm pillar configuration displayed more substantial decreases of 9.2%. Notably, the 350 µm pillar configuration consistently yielded higher permeability than those with smaller diameters, regardless of pressure. However, the 350 µm pillar configuration underwent a 11.2% decline over the same pressure range. While the absolute permeability was higher for larger pillar configurations, they also exhibited greater relative loss, indicating that increasing the pillar diameter leads to less hydrodynamic resistance and promotes efficient flow pathways.

This trend is reinforced as porosity increased to 0.55 (Figure 4.2), as a similar trend was observed, but with slightly more pronounced decreases. The permeability of the 250 µm pillars dropped by 10.1%, whereas the 300 µm and 350 µm pillars showed reductions of 12.8% and 18.1%, respectively. This indicates that while a more porous medium supports higher initial permeability, it may also be more susceptible to pressure-induced reductions.

At the highest porosity of 0.60 (Figure 4.3), the relative change in permeability became even more evident. The 250 µm pillars showed a 15.8% drop, the 300 µm pillars decreased by 23.1%, and the 350 µm pillars exhibited the largest reduction of approximately 26% from 10 to 40 mbar. These results show that as porosity increases, the structure becomes more vulnerable to pressure-related flow degradation, particularly in systems with larger pillar sizes.

Larger pillars consistently offer higher permeability under all conditions due to reduced flow obstruction. However, systems with higher porosity and larger pillars exhibit a more significant percentage decline in permeability with increasing pressure due to increased sensitivity of flow pathways to pressure gradients. This indicates a trade-off between achieving high permeability and maintaining flow stability under pressure. Additionally, increased porosity led to higher permeability values, as expected, due to the greater fraction of void space available for fluid flow.

These results highlight that optimizing both pillar diameter and porosity both enhance permeability across all pressures studied and is essential for improving flow performance in microfluidic filtration systems. These findings underscore the importance of carefully designing pillar architectures in microfluidic filtration applications particularly in processes susceptible to cake layer compaction from soft particles where maintaining stable permeability is essential.

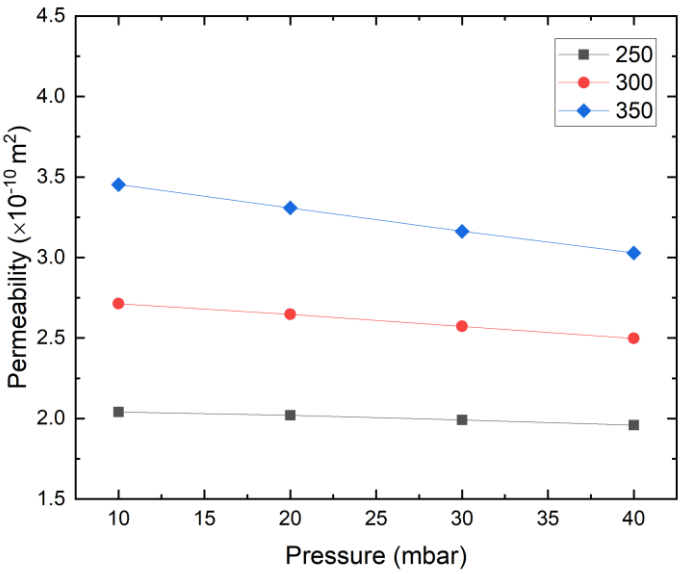

Figure 4.1. Comparison of permeabilities obtained from numerical simulation against static inlet pressure for different pillar size of disordered configurations of circular micropillars at a minimum pore throat of 50 µm and 0.5 porosity.

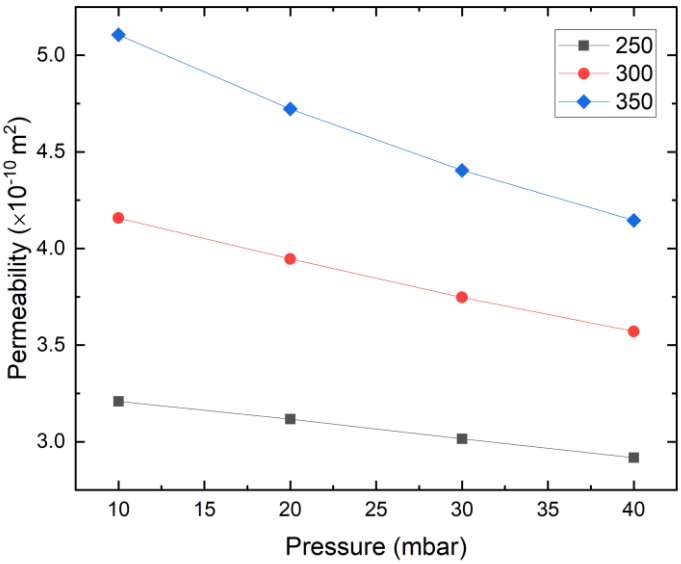

Figure 4.2. Comparison of permeabilities obtained from numerical simulation against static inlet pressure for different pillar size of disordered configurations of circular micropillars at a minimum pore throat of 50 µm and 0.55 porosity.

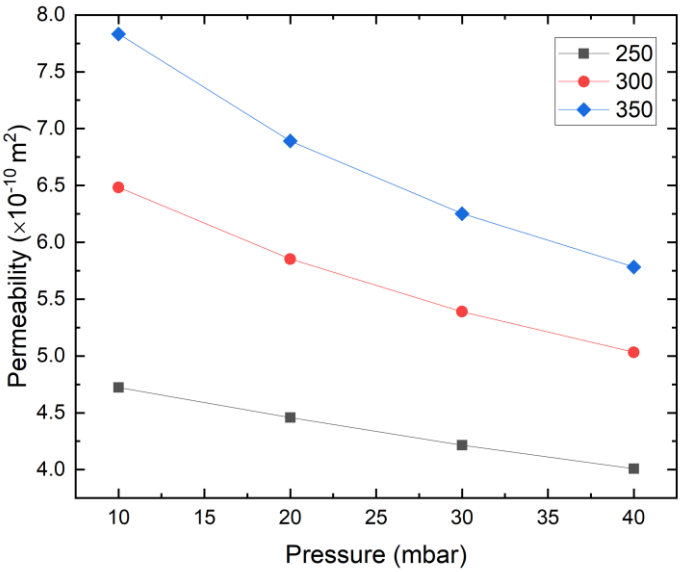

Figure 4.3. Comparison of permeabilities obtained from numerical simulation against static inlet pressure for different pillar size of disordered configurations of circular micropillars at a minimum pore throat of 50 µm and 0.6 porosity.

4.2 Effect of Pore Throat Size on Permeability

The effect of pore throat size on permeability was investigated considering pore throat sizes of 50, 60, and 70 µm. Simulations were carried out at a fixed pillar diameter of 350 µm and under inlet pressures of 10, 20, 30, and 40 mbar. The findings corresponding to porosity values of 0.50, 0.55, and 0.60 are illustrated in Figures 4.1, 4.2, and 4.3, respectively.

While porosity largely determines the overall scale of permeability, the pore throat, which is defined as the spacing between pillars, plays a critical role in regulating local hydraulic resistance. The data clearly demonstrate that for a given porosity, permeability is highly sensitive to the pore throat size. As illustrated in Figures 4.4, 4.5, and 4.6, the data series for pore throats of 50, 60, and 70 µm consistently show that a larger minimum pore throat size results in higher permeability. This trend is evident across all porosity values. For example, in Figure 4.5 at 0.55 porosity, increasing the pore throat size from 50 µm to 70 µm at 10 mbar raises the permeability from 5.1×10^{-10} m^2 to 5.8×10^{-10} m^2, representing an approximate 15% increase. These pore throats act as primary constriction points where velocity peaks and viscous dissipation are most intense. Therefore, widening the pore throat alleviates local flow resistance and enhances overall permeability.

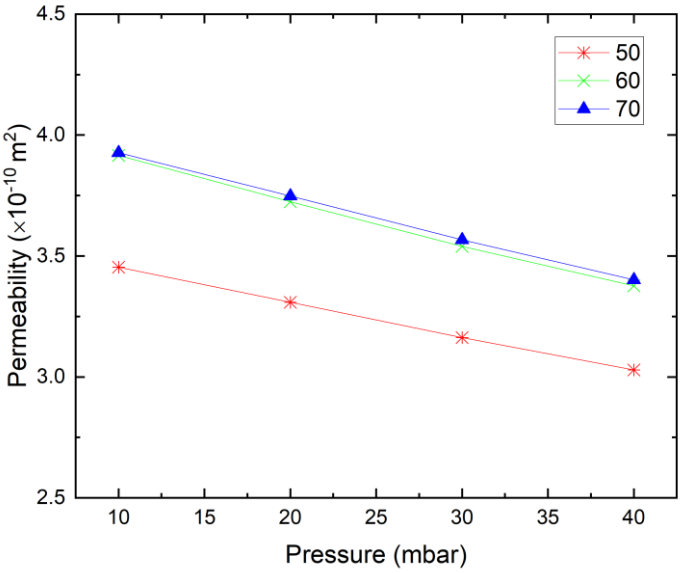

Figure 4.4. Comparison of permeabilities obtained from numerical simulation against static inlet pressure for different pore throat sizes of disordered configurations of circular micropillars at a pillar diameter of 350 µm and 0.5 porosity.

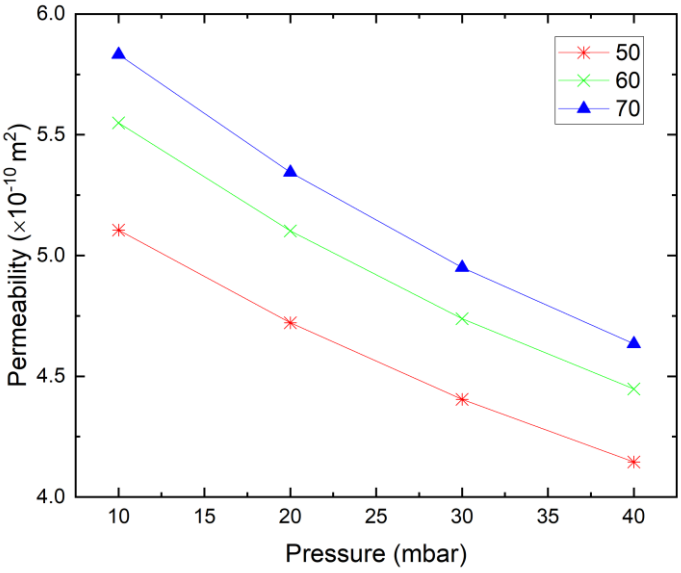

Figure 4.5. Comparison of permeabilities obtained from numerical simulation against static inlet pressure for different pore throat sizes of disordered configurations of circular micropillars at a pillar diameter of 350 µm and 0.55 porosity

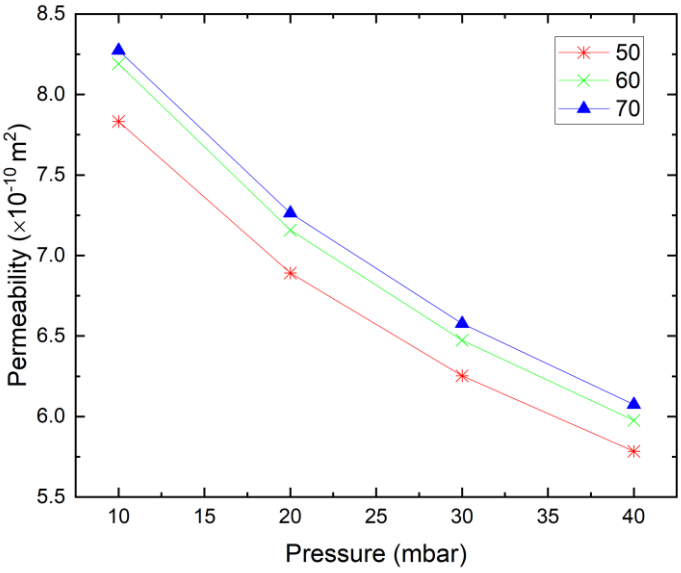

Figure 4.6. Comparison of permeabilities obtained from numerical simulation against static inlet pressure for different pore throat sizes of disordered configurations of circular micropillars at a pillar diameter of 350 µm and 0.6 porosity.

4.3 Effect of Porosity on Permeability

A comparative analysis across Figures 4.4, 4.5, and 4.6, demonstrates that increasing the void fraction of the medium leads to a substantial enhancement in permeability. For a fixed pillar diameter of 350 μm and a constant pore throat of 70 μm, the permeability at an applied pressure of 10 mbar increases from approximately 3.9×10^{-10} m^2 at porosity of 0.5 (Figure 4.4) to 5.8×10^{-10} m^2 at porosity of 0.55 (Figure 4.5), and further to 8.3×10^{-10} m^2 at porosity of 0.6 (Figure 4.6). This represents a more than two-fold increase in permeability over a porosity range of just 0.1. This observation aligns with the established principle that increased void space facilitates more open and less resistant flow channels, thereby lowering overall hydraulic resistance. A similar non-linear dependence of permeability on porosity has also been reported in previous numerical studies of microstructured porous media (Nie et al., 2024).

To contextualize these simulation findings, the computed permeability was compared with predictions from three prominent theoretical and semi-empirical models. These include the KC equation, the model by Koch and Ladd (KL), and a model introduced by Yazdchi et al. (YSL). The comparison, shown in Figure 4.7 for a pillar diameter of 300 μm and a pore throat of 60 μm, reveals notable quantitative discrepancies, highlighting the challenges associated with accurately modelling and predicting flow behavior in geometries of such complexity.

All three theoretical models succeed to predict the qualitative trend of increasing permeability with increasing porosity. Nevertheless, their predictive quantitative accuracy shows considerable variation. The KC equation, although providing a reasonable order-of-magnitude estimate, tends to predict lower permeability values compared to the simulated permeabilities. This is not surprising, as the KC model was originally formulated for packed beds of granular particles and its derivation relies on assumptions of creeping flow and a simplified geometric representation that often does not adequately reflect the structural characteristics of complex porous systems such as disordered pillar arrays.

The model introduced by (Yazdchi et al., 2011). (YSL), which is often presented as a modification of the KC equation that better accounts for tortuosity in fibrous media, shows the closest agreement with the simulation results. This improved accuracy suggests that a more refined treatment of the tortuous flow paths, which are a dominant feature of the pillar arrays, is critical for accurate permeability prediction.

Most strikingly, the (Koch & Ladd, 1997) model overpredicts the permeability, exceeding simulation results by more than an order of magnitude. This model was originally developed for specific geometric configurations and flow regimes, primarily focusing on periodic square arrays and random arrays of aligned cylinders and extending the analysis beyond creeping flow to include inertial effects (Koch & Ladd, 1997). The vast discrepancy observed in this study indicates that the specific formulation of the KL model applied here does not accurately represent the flow behaviour within densely packed, disordered pillar configurations. In such systems, the resistance to flow is primarily influenced by complex hydrodynamic interactions arising from the close proximity of the pillars. This comparison highlights the fact that, although theoretical models can provide valuable physical insight, their predictive accuracy is limited by their underlying assumptions. Therefore, DNS remains an essential tool for accurately characterizing and analyzing flow behavior in media with complex microstructural features.

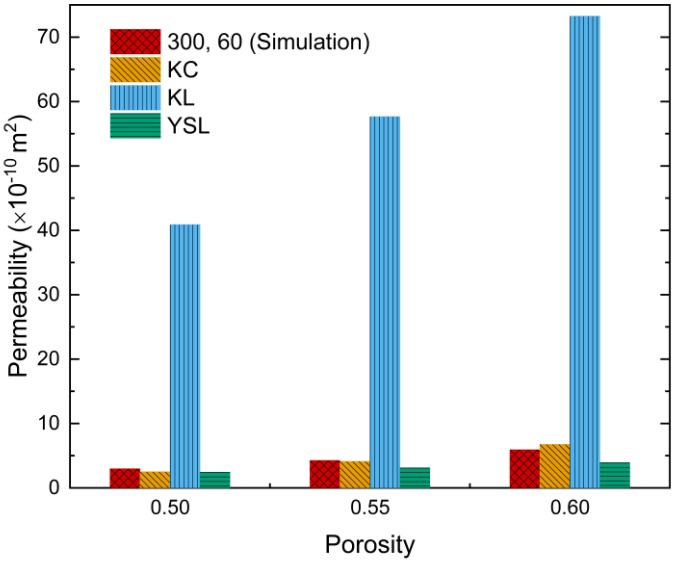

Figure 4.7. Comparison of permeabilities obtained from numerical with theoretical and semi-empirical models for a pillar diameter of 300 µm and a pore throat of 60 µm.

4.4 Pressure-Dependent Permeability: Evidence of Non-Darcian Flow

A notable and consistent trend observed across all simulated configurations is the near-linear decrease in calculated permeability as the applied pressure drop across the microfluidic device increases from 10 mbar to 40 mbar. This behaviour marks a significant deviation from the classical Darcy's Law. The later states that permeability is an intrinsic property of a porous medium, independent of the pressure gradient or flow rate. This law is fundamental to the study of porous media but is strictly valid only under conditions of slow, viscous dominated (creeping) flow regime, where the Reynolds number is low.

The observed negative slope in the permeability-pressure plots indicates that the hydraulic resistance increases as the fluid flow rate, driven by pressure, increases. This trend indicates the onset of inertial effects, even though the Reynolds numbers remain relatively low. In such conditions, inertial forces, while still small compared to viscous forces, become non-negligible, leading to deviations from linear pressure–flow behavior. Darcy's law assumes a perfectly linear relationship between flow rate (Q) and pressure drop (ΔP). However, when the actual pressure required to maintain a given flow rate is higher than predicted by this linear model, the permeability decreases with increasing pressure. This effect is a well-known hallmark of non-Darcian flow. Such behavior implies that the flow regime is transitioning toward one where fluid inertia contributes meaningfully to energy losses, even if laminar conditions are still dominant, a phenomenon often modelled with extensions to Darcy's law like the Brinkman or Forchheimer equations. These equations introduce inertial corrections or effective viscosity terms, allowing for better characterization of flow in complex microstructured geometries like micropillar arrays. This phenomenon has also been examined in the literature, including studies on the permeability of disordered pillar arrays in microfluidic devices, such as the work by

Chakrapani (2023), which applied Brinkman's theory to capture the effects of wall friction and non-Darcian behavior.

Although the overall flow in microfluidic devices is typically laminar, the disordered micropillars arrangement introduces significant geometric complexity, resulting in highly tortuous and non-linear streamlines. Rather than progressing along straight paths, the fluid is forced to navigate a network of frequent expansions and contractions between pillars, continuously altering its direction and velocity. This intricate flow topology increases local shear gradients and energy dissipation, which can significantly influence transport properties such as permeability and pressure drop.

The underlying cause of the observed non-Darcian flow behavior is rooted in the fundamental principles of fluid dynamics described by the Navier-Stokes equations. Darcy's Law is a simplification of these equations, valid only when the inertial term, $\rho(u \cdot \nabla)u$, is negligible. This term represents the convective acceleration of the fluid. In the case of the pillar arrays examined in this study, as fluid accelerates through the narrow pore throats and subsequently decelerates in the more open regions between pillars, making the inertial effects becomes significant. Such variations in velocity demand an input of energy, which is supplied by the pressure gradient driving the flow. This dissipation of kinetic energy is a loss mechanism that is entirely separate from the viscous friction accounted for in Darcy's Law.

4.5 Flow Field Analysis: Velocity Distribution and Streamline Patterns

To further reveal the influence of the pillar arrangement on the permeability and internal fluid dynamics, the velocity fields and corresponding streamlines were simulated for three distinct porous media configurations of different pillar diameters and pore throats. Figure 4.8 presents a comparative visualization of these simulations, conducted at a constant inlet pressure of 40 mbar. Each configuration is defined by its pillar diameter, minimum pore throat, and porosity, respectively. The analysis focuses on understanding how these geometric parameters govern the flow paths and velocity magnitudes, which are precursors to predicting permeability and potential fouling behavior.

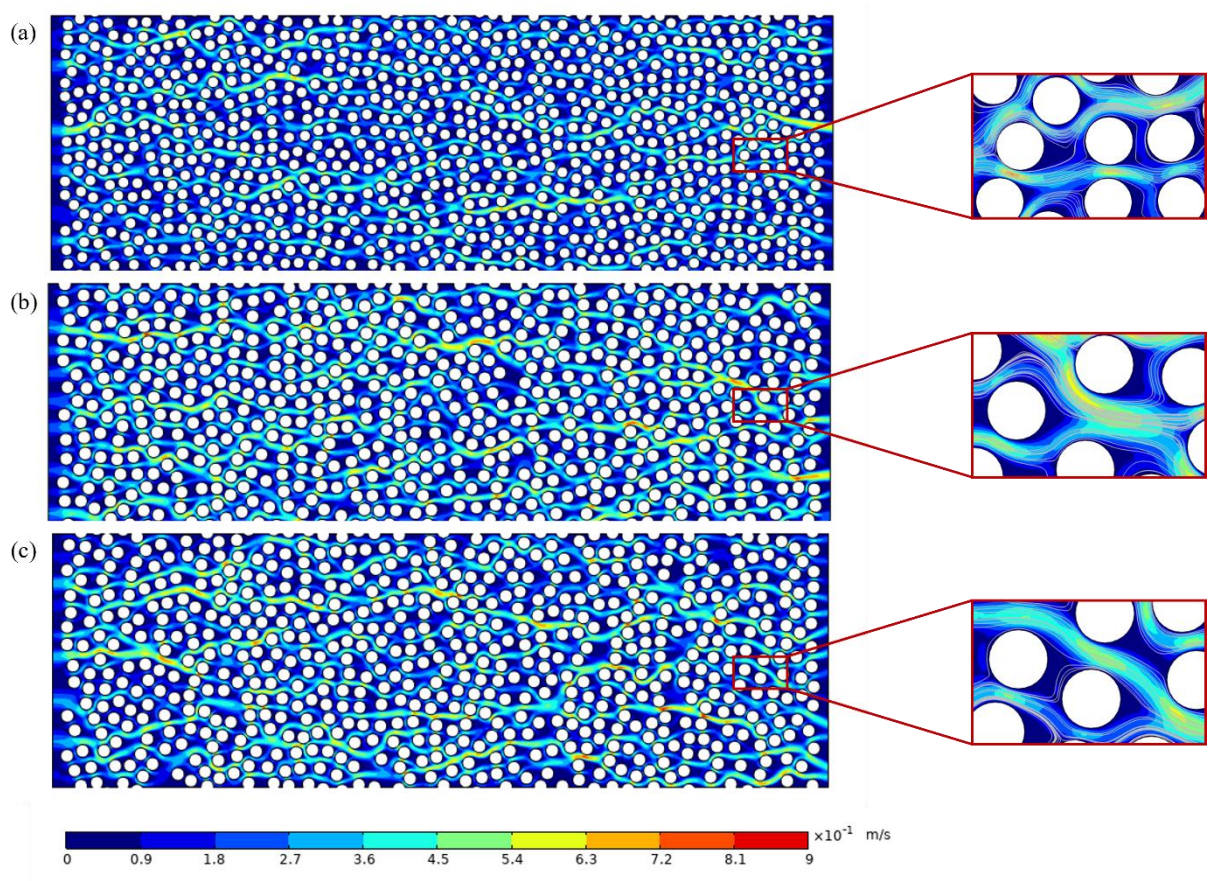

Figure 4.8. Velocity distributions (left) and streamline patterns (right) for pillar arrangements: (a) 300, 60, 0.6; (b) 350, 60, 0.6; and (c) 350, 50, 0.6. The colour legend represents the velocity magnitude (in m/s) of the horizontal velocity field at an inlet pressure of 40 mbar.

A comparison between configurations (a) and (b) highlights the effect of the pillar diameter on flow behaviour. Interestingly, the structure with larger pillars, (b), produced a higher maximum local velocity of 0.856m/s compared to 0.74m/s in configuration (a). This finding suggests that while the porosity and minimum pore throat are held constant, the larger pillars in (b) induce more significant flow heterogeneity. The fluid is routed into a few preferential channels where velocity is increased, which consequently expands the low-velocity, near-stagnant zones. In contrast, the flow in (a) appears less heterogeneously distributed than (b), characterized by a lower velocity range across the domain.

The effect of the minimum pore throat size is assessed by comparing configurations (b) and (c). As anticipated, reducing the minimum pore throat from 60µm to 50µm resulted in the highest maximum local velocity of all three arrangements, reaching 0.863m/s in configuration (c). This acceleration arises from the principle of mass continuity (conservation of mass), which necessitates increased fluid velocity at narrower constrictions to maintain a constant volumetric flow rate. The streamlines shown in the magnified view of Figure 4.8c exhibit more compression through these bottlenecks, which is indicative of more tortuous and accelerated flow paths.

A crucial observation across all three arrangements is the furcate nature of the flow. The disordered pillar placement creates complex, branching streamlines that increase the effective path

length for fluid seepage, a key contributor to overall hydrodynamic resistance. This disordered structure promotes the formation of preferential flow paths, a phenomenon often termed "channelling," which is evident in all configurations.

From these velocity profiles, direct implications for permeability can be drawn. The results reveal that arrangements with more defined preferential channels are not necessarily less permeable. In fact, configuration (b) exhibited the highest permeability. Surprisingly, configuration (a), with its more evenly distributed flow, was the most resistant to flow, possessing a permeability that was only about 88% of that measured for configuration (b). Meanwhile, configuration (c), whose narrow pore throats created the highest-velocity streams, presented a greater overall resistance to flow than (b), with a permeability that was approximately 97% of that measured for configuration (b). This finding underscores that the overall permeability is dictated by the global structure of the pillar network rather than solely by the maximum velocity in localized constrictions or the uniformity of the flow. Therefore, a system with well-defined but not excessively constrictive channels, like (b), is more permeable than both a system with less heterogeneous flow (a) and one with more significant constrictions (c).

From a design perspective, this analysis provides valuable insight into the optimisation of microfluidic membranes for filtration applications aimed at minimising soft particle accumulation. Reducing stagnation zones while ensuring consistent, well-connected flow channels is critical to maintaining high permeability and preventing excessive cake layer formation. Moreover, achieving an optimal trade-off between structural randomness, channelling, and pore throat size may offer a viable method for optimising both permeability and fouling resistance in filtration systems.

4.6 Pressure Analysis: Effect of Pillar Geometry on Pressure Drop and Flow

Investigation of the pressure distribution across the three pillar arrangements provides insight into the geometric factors governing hydraulic resistance. The hydraulic resistance of each pillar arrangement was evaluated by measuring the pressure drop across the chip at a normal inflow velocity of 0.1. As depicted in Figure 4.9, all configurations exhibit a characteristic pressure gradient, with pressure decreasing linearly along the direction of flow from the inlet (left) to the outlet (right). A quantitative comparison revealed that configuration (a), which features a pillar diameter of 300 µm and a minimum pore throat of 60 µm, generated the largest pressure drop of 41 mbar. In contrast, configurations (c) and (b) yielded a lower pressure drop of about 35.9 and 34 mbar, respectively.

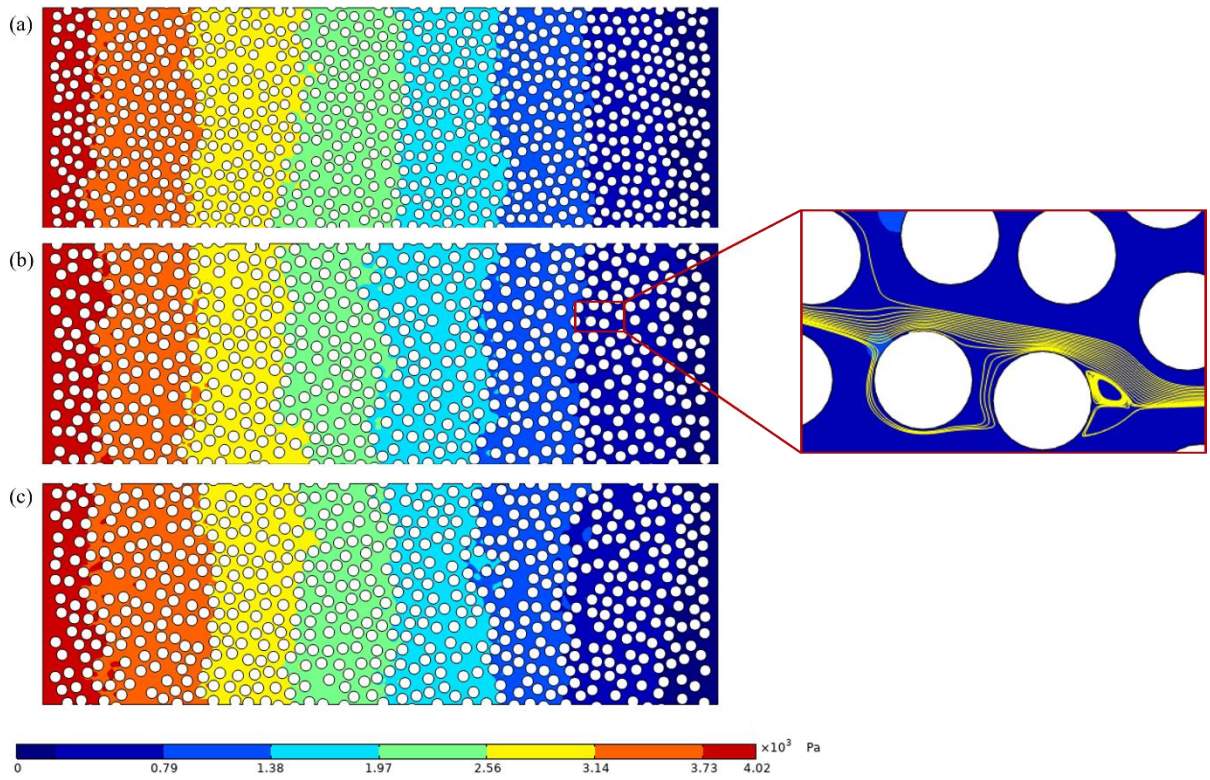

Figure 4.9. Pressure distribution (left) and pressure drop streamline (right) for pillar arrangements: (a) 300, 60, 0.6; (b) 350, 60, 0.6; and (c) 350, 50, 0.6. The colour legend represents the pressure values (in Pa).

This comparison highlights that the pillar size is the dominant parameter controlling the overall flow resistance. The reduction of the pillar diameter from 350 µm in configuration (b) to 300 µm in configuration (a) is directly responsible for the significant increase in pressure drop. On the other hand, the increase in the minimum pore throat size from 50 µm (c) to 60 µm (b), while keeping the pillar size constant, had a minor or negligible impact on the overall pressure drop.

Further analysis of the flow kinematics, illustrated by the streamline in Figure 4.9b, revealed the underlying mechanism behind the observed pressure loss and its implications for membrane fouling. As the fluid accelerates through the narrow constrictions between pillars, flow separation occurs in the downstream region of the pillars. This leads to the formation of stable, recirculating eddies or vortices in the low-velocity zones behind pillars. These eddies are not part of the main, through-flowing fluid but are sustained by energy transferred from it via shear forces. This process represents an additional energy dissipation mechanism, known as form drag, which contributes to the total pressure drop (Koch & Ladd, 1997; Nield, 1991). The presence of these inertial effects explains why the relationship between flow velocity and pressure gradient in such geometries is often non-linear, as the size and intensity of these energy-dissipating eddies typically increase with flow velocity.

Beyond hydraulic resistance, these eddies also act as hydrodynamic traps, entraining suspended particles and significantly increasing their local residence time. This prolonged exposure raises the likelihood that soft or deformable particles will adhere to pillar surfaces or aggregate,

thereby initiating fouling and cake layer formation. The presence and behaviour of these vortices are strongly influenced by the geometry of the pillar arrangement, and their size and intensity typically increase with flow velocity. This explains the non-linear relationship between flow rate and pressure gradient observed in such geometries.

Therefore, optimal membrane design should not focus solely on minimizing the clean-fluid pressure drop but also aim to reduce the size and stability of these recirculating zones. By engineering a more uniform and streamlined flow field, the design can discourage particle accumulation, minimize fouling, and enhance the long-term operational performance of the filtration system.

5 Conclusion

This study successfully characterized the hydrodynamic behavior of microfluidic membranes with disordered micropillar arrays, providing fundamental insights into the factors governing fluid flow in such microstructures. The permeability of the micropillar arrays is strongly influenced by their geometric design, with increases in pillar diameter, pore throat size, and porosity all leading to higher baseline permeability and lower hydraulic resistance. However, the most significant finding of this work is the clear evidence of non-Darcian flow. Across all simulated configurations, the calculated permeability exhibited a near-linear decrease with increasing applied pressure, dropping by as much as 26% in some cases, a key deviation from classical Darcy's Law. This phenomenon is attributed to the growing influence of inertial forces, which become non-negligible as fluid accelerates and decelerates through the tortuous paths of the pillar array. Analysis of the simulated flow fields revealed that these inertial effects result in significant flow heterogeneity, including preferential channelling and the formation of stable, recirculating eddies. These eddies contribute to energy dissipation through form drag and increase the local residence time of particles, which raises the likelihood of their adhesion to pillar surfaces. It was further determined that the overall permeability is dictated by the global structure of the pillar network rather than solely by localized constrictions. Finally, a comparison with established theoretical models revealed significant quantitative discrepancies, underscoring their limitations and validating the necessity of DNS for precise characterization. In summary, this research demonstrates that optimizing membrane performance requires a holistic design approach that considers the entire microstructural architecture to minimize detrimental inertial effects and enhance long-term operational stability.

6 Future Studies

To build upon the findings of this thesis, several areas are recommended for future investigation. A direct experimental comparison is necessary to validate the numerical results. This should involve conducting pure water flux experiments with the already fabricated devices and implementing micro-PIV to measure the actual velocity fields. To more accurately simulate the filtration of soft particles, the current CFD model should be extended to include a Fluid-Structure Interaction (FSI) module, allowing for the modelling of deformable particles and their compression under hydrodynamic forces. The combination of FSI simulations with µPIV validation would represent a particularly powerful approach. Finally, a detailed study focusing on the observed non-Darcian flow is warranted. This could involve applying Brinkman's theory to the simulation results to better model the effective viscosity and capture the transition from Darcy to non-Darcian flow, allowing for the prediction of filtration performance and permeability in microfilters through modelled equations, in particular for disordered pillar arrays in microfluidic membranes.

References

Anbari, A., Chien, H. T., Datta, S. S., Deng, W., Weitz, D. A. & Fan, J. (2018). Microfluidic Model Porous Media: Fabrication and Applications, *Small*

Anushka, Bandopadhyay, A. & Das, P. K. (2023). Paper Based Microfluidic Devices: A Review of Fabrication Techniques and Applications, *European Physical Journal: Special Topics*

Ben Hassan, I., Lafforgue, C., Ayadi, A. & Schmitz, P. (2014). In Situ 3D Characterization of Monodispersed Spherical Particle Deposition on Microsieve Using Confocal Laser Scanning Microscopy, *Journal of Membrane Science*, vol. 454, pp.283–297

Benet, E., Badran, A., Pellegrino, J. & Vernerey, F. (2017). The Porous Media's Effect on the Permeation of Elastic (Soft) Particles, *Journal of Membrane Science*, vol. 535, pp.10–19

Bouhid de Aguiar, I., Meireles, M., Bouchoux, A. & Schroën, K. (2019). Microfluidic Model Systems Used to Emulate Processes Occurring during Soft Particle Filtration, *Scientific Reports*, vol. 9, no. 1

Cao, Z., Liu, G., Zhan, H., Li, C., You, Y., Yang, C. & Jiang, H. (2016). Pore Structure Characterization of Chang-7 Tight Sandstone Using MICP Combined with N 2 GA Techniques and Its Geological Control Factors, *Scientific Reports*, vol. 6

Chew, J. W., Kilduff, J. & Belfort, G. (2020). The Behavior of Suspensions and Macromolecular Solutions in Crossflow Microfiltration: An Update, *Journal of Membrane Science*

Cirillo, A. I., Tomaiuolo, G. & Guido, S. (2021). Membrane Fouling Phenomena in Microfluidic Systems: From Technical Challenges to Scientific Opportunities, *Micromachines*

Cirillo, A. I., Tomaiuolo, G. & Guido, S. (2023). Microfiltration of Concentrated Albumin Solutions and the Role of Processing Conditions on Membrane Fouling, *Chemical Engineering Journal Advances*, vol. 16

de Aguiar, I. B. & Schroën, K. (2020a). Microfluidics Used as a Tool to Understand and Optimize Membrane Filtration Processes, *Membranes*

de Aguiar, I. B. & Schroën, K. (2020b). Microfluidics Used as a Tool to Understand and Optimize Membrane Filtration Processes, *Membranes*

de Winter, D. A. M., Weishaupt, K., Scheller, S., Frey, S., Raoof, A., Hassanizadeh, S. M. & Helmig, R. (2021). The Complexity of Porous Media Flow Characterized in a Microfluidic Model Based on Confocal Laser Scanning Microscopy and Micro-PIV, *Transport in Porous Media*, vol. 136, no. 1, pp.343–367

Debnath, N. & Sadrzadeh, M. (2018). Microfluidic Mimic for Colloid Membrane Filtration: A Review, *Journal of the Indian Institute of Science*

Fallahi, H., Zhang, J., Phan, H. P. & Nguyen, N. T. (2019). Flexible Microfluidics: Fundamentals, Recent Developments, and Applications, *Micromachines*

Ferreira, M., Carvalho, V., Ribeiro, J., Lima, R. A., Teixeira, S. & Pinho, D. (2024). Advances in Microfluidic Systems and Numerical Modeling in Biomedical Applications: A Review, *Micromachines*

Gerami, A., Mostaghimi, P., Armstrong, R. T., Zamani, A. & Warkiani, M. E. (2016). A Microfluidic Framework for Studying Relative Permeability in Coal, *International Journal of Coal Geology*, vol. 159, pp.183–193

Giiell, C. & Davis, R. H. (1996). Membrane Fouling during Microfiltration of Protein Mixtures, *Journal of Membrane Science*, Vol. 119

Goswami, I., Kim, Y., Neiman, G., Siemons, B., Velazquez, J. I., Yazgan, K., Ng, T. & Healy, K. E. (2025). Pillar Arrays as Tunable Interfacial Barriers for Microphysiological Systems, Available Online: http://biorxiv.org/lookup/doi/10.1101/2025.01.08.632020

Gräfner, S. J., Wu, P. Y. & Kao, C. R. (2022). Flow in a Microchannel Filled with Arrays of Numerous Pillars, *International Journal of Heat and Fluid Flow*, vol. 97

Hale, R. S., Bonnecaze, R. T. & Hidrovo, C. H. (2014a). Optimization of Capillary Flow through Square Micropillar Arrays, *International Journal of Multiphase Flow*, vol. 58, pp.39–51

Hale, R. S., Ranjan, R. & Hidrovo, C. H. (2014b). Capillary Flow through Rectangular Micropillar Arrays, *International Journal of Heat and Mass Transfer*, vol. 75, pp.710–717

He, S., Joseph, N., Feng, S., Jellicoe, M. & Raston, C. L. (2020). Application of Microfluidic Technology in Food Processing, *Food and Function*

Hinderink, E. B. A., de Ruiter, J., de Leeuw, J., Schroën, K., Sagis, L. M. C. & Berton-Carabin, C. C. (2021). Early Film Formation in Protein-Stabilised Emulsions: Insights from a Microfluidic Approach, *Food Hydrocolloids*, vol. 118

Hulikal Chakrapani, T., Bazyar, H., Lammertink, R. G. H., Luding, S. & den Otter, W. K. (2022). The Permeability of Pillar Arrays in Microfluidic Devices: An Application of Brinkman's Theory towards Wall Friction, *Soft Matter*, vol. 19, no. 3, pp.436–450

Jahanbakhsh, A., Wlodarczyk, K. L., Hand, D. P., Maier, R. R. J. & Maroto-Valer, M. M. (2020). Review of Microfluidic Devices and Imaging Techniques for Fluid Flow Study in Porous Geomaterials, *Sensors (Switzerland)*

Karimifard, S., Li, X., Elowsky, C. & Li, Y. (2021). Modeling the Impact of Evolving Biofilms on Flow in Porous Media inside a Microfluidic Channel, *Water Research*, vol. 188

Kaufman, Y., Kasher, R., Lammertink, R. G. H. & Freger, V. (2012). Microfluidic NF/RO Separation: Cell Design, Performance and Application, *Journal of Membrane Science*, vol. 396, pp.67–73

Koch, D. L. & Ladd, A. J. C. (1997). Moderate Reynolds Number Flows through Periodic and Random Arrays of Aligned Cylinders, *Journal of Fluid Mechanics*, vol. 349, pp.31–66

Lin, L. & Chung, C. K. (2021). PDMS Microfabrication and Design for Microfluidics and Sustainable Energy Application: Review, *Micromachines*

Linkhorst, J., Beckmann, T., Go, D., Kuehne, A. J. C. & Wessling, M. (2016). Microfluidic Colloid Filtration, *Scientific Reports*, vol. 6

Lipnizki, F. & Dupuy, A. (2013). Food Industry Applications, *Encyclopedia of Membrane Science and Technology*, [e-journal] pp.1–23, Available Online: https://onlinelibrary.wiley.com/doi/full/10.1002/9781118522318.emst126 [Accessed 28 July 2025]

Lipnizki, F., Thuvander, J. & Rudolph, G. (2019). Membrane Processes and Applications for Biorefineries, in *Current Trends and Future Developments on (Bio-) Membranes: Membranes in Environmental Applications*, Elsevier Inc., pp.283–301

Lipnizki, F., Thuvander, J. & Rudolph-Schöpping, G. (2023). Protein Shift – How Membrane Technology Can Contribute, *Chemie-Ingenieur-Technik*, vol. 95, no. 9, pp.1403–1408

Lüken, A. (2022). From Soft Matter Filtration Processes to Microfluidic Filter Cake Visualization, *Aachener Verfahrenstechnik Series AVT.CVT-Chemical Process Engineering*, vol. 30

Lüken, A., Linkhorst, J., Fröhlingsdorf, R., Lippert, L., Rommel, D., De Laporte, L. & Wessling, M. (2020). Unravelling Colloid Filter Cake Motions in Membrane Cleaning Procedures, *Scientific Reports*, vol. 10, no. 1

Lüken, A., Stüwe, L., Lohaus, J., Linkhorst, J. & Wessling, M. (2021). Particle Movements Provoke Avalanche-like Compaction in Soft Colloid Filter Cakes, *Scientific Reports*, vol. 11, no. 1

Massimiani, A., Panini, F., Marasso, S. L., Cocuzza, M., Quaglio, M., Pirri, C. F., Verga, F. & Viberti, D. (2023). 2D Microfluidic Devices for Pore-Scale Phenomena Investigation: A Review, *Water (Switzerland)*

Mohammadi, M. & Riazi, M. (2022). Applicable Investigation of SPH in Characterization of Fluid Flow in Uniform and Non-Uniform Periodic Porous Media, *Sustainability (Switzerland)*, vol. 14, no. 21

Mu, R., Bu, N., Pang, J., Wang, L. & Zhang, Y. (2022). Recent Trends of Microfluidics in Food Science and Technology: Fabrications and Applications, *Foods*

Muijlwijk, K., Berton-Carabin, C. & Schroën, K. (2016). Cross-Flow Microfluidic Emulsification from a Food Perspective, *Trends in Food Science & Technology*, [e-journal] vol. 49, pp.51–63, Available Online: https://www.sciencedirect.com/science/article/pii/S0924224416000030 [Accessed 28 July 2025]

Musabbir Rahman, R., Niemur, E., Blois, G., Kazemifar, F., Kim, M. & Li, Y. (2025). A Novel Microfluidic Approach to Quantify Pore-Scale Mineral Dissolution in Porous Media, *Scientific Reports*, vol. 15, no. 1

Ngene, I. S., Lammertink, R. G. H., Wessling, M. & van der Meer, W. (2010). A Microfluidic Membrane Chip for in Situ Fouling Characterization, *Journal of Membrane Science*, vol. 346, no. 1, pp.202–207

Ngene, I. S., Lammertink, R. G. H., Wessling, M. & Van der Meer, W. G. J. (2011). Visual Characterization of Fouling with Bidisperse Solution, *Journal of Membrane Science*, vol. 368, no. 1–2, pp.110–115

Nie, S., Liu, P., Chen, K., Wang, W., Chen, Y. & Bate, B. (2024). Permeability of Structured Porous Media: Numerical Simulations and Microfluidic Models, *Journal of Zhejiang University: Science A*, vol. 25, no. 12, pp.1018–1036

Nield, D. A. (1991). The Limitations of the Brinkman-Forchheimer Equation in Modeling Flow in a Saturated Porous Medium and at an Interface

Rahmanian, M., Sartipzadeh Hematabad, O., Askari, E., Shokati, F., Bakhshi, A., Moghadam, S., Olfatbakhsh, A., Al Sadat Hashemi, E., Khorsand Ahmadi, M., Morteza Naghib, S., Sinha, N., Tel, J., Eslami Amirabadi, H., den Toonder, J. M. J. & Majidzadeh-A, K. (2023). A Micropillar Array-Based Microfluidic Chip for Label-Free Separation of Circulating Tumor Cells: The Best Micropillar Geometry?, *Journal of Advanced Research*, vol. 47, pp.105–121

Rudolph, G., Virtanen, T., Ferrando, M., Güell, C., Lipnizki, F. & Kallioinen, M. (2019). A Review of in Situ Real-Time Monitoring Techniques for Membrane Fouling in the Biotechnology, Biorefinery and Food Sectors, *Journal of Membrane Science*

Schroën, K. & Bouhid de Aguiar, I. (2023). Rethinking Membrane Processes for Food: From Particle Behavior to Innovative Membrane Cascades, *Chemie-Ingenieur-Technik*, vol. 95, no. 9, pp.1388–1393

Schroën, K. & Bouhid de Aguiar, I. (2024). The Under-Recognized Fundamental Effects of Component Interaction and Deformability for Membrane Processes for Food, *Separation and Purification Technology*

Schroën, K., de Ruiter, J. & Berton-Carabin, C. C. (2020). Microtechnological Tools to Achieve Sustainable Food Processes, Products, and Ingredients, *Food Engineering Reviews*

Stüwe, L., Lüken, A., Stockmeier, F., Griesberg, L., Kratzenberg, T., Linkhorst, J., Richtering, W. & Wessling, M. (2024). Temporal Resistance Fluctuations during the Initial Filtration Period of Colloidal Matter Filtration, *Journal of Membrane Science*, vol. 708

Tamayol, A., Khosla, A., Gray, B. L. & Bahrami, M. (2012). Creeping Flow through Ordered Arrays of Micro-Cylinders Embedded in a Rectangular Minichannel, *International Journal of Heat and Mass Transfer*, vol. 55, no. 15–16, pp.3900–3908

Valencia, A., LeMen, C., Ellero, C., Lafforgue-Baldas, C., F. Morris, J. & Schmitz, P. (2022). Direct Observation of the Microfiltration of Yeast Cells at the Micro-Scale: Characterization of Cake Properties, *Separation and Purification Technology*, vol. 298

Wang, H. & Wang, P. (2017). An Experimental Investigation of the Permeability in Porous Chip Formed by Micropost Arrays Based on Microparticle Image Velocimetry and

Micromanometer Measurements, *Journal of Fluids Engineering, Transactions of the ASME*, vol. 139, no. 2

Wang, L., Li, Y., Zhao, G., Chen, N. & Xu, Y. (2019). Experimental Investigation of Flow Characteristics in Porous Media at Low Reynolds Numbers (Re→0) under Different Constant Hydraulic Heads, *Water (Switzerland)*, vol. 11, no. 11

Xia, Y., Goral, J., Huang, H., Miskovic, I., Meakin, P. & Deo, M. (2017). Many-Body Dissipative Particle Dynamics Modeling of Fluid Flow in Fine-Grained Nanoporous Shales, *Physics of Fluids*, vol. 29, no. 5

Yazdchi, K., Srivastava, S. & Luding, S. (2011). Microstructural Effects on the Permeability of Periodic Fibrous Porous Media, *International Journal of Multiphase Flow*, vol. 37, no. 8, pp.956–966

Yazdchi, K., Srivastava, S. & Luding, S. (2012). Micro-Macro Relations for Flow through Random Arrays of Cylinders, *Composites Part A: Applied Science and Manufacturing*, vol. 43, no. 11, pp.2007–2020

Zhou, L., Zhang, Y., Deng, X. & Liu, M. (2016). Dissipative Particle Dynamics Simulation of Flow through Periodic Arrays of Circular Micropillar, *Applied Mathematics and Mechanics (English Edition)*, vol. 37, no. 11, pp.1431–1440